science.sciencemag.org/content/371/6531/839/suppl/DC1

Supplementary Materials for

Cholangiocyte organoids can repair bile ducts after transplantation in the human liver

Fotios Sampaziotis*, Daniele Muraro, Olivia C. Tysoe, Stephen Sawiak, Timothy E. Beach, Edmund M. Godfrey, Sara S. Upponi, Teresa Brevini, Brandon T. Wesley, Jose Garcia-Bernardo, Krishnaa Mahbubani, Giovanni Canu, Richard Gieseck III, Natalie L. Berntsen, Victoria L. Mulcahy, Keziah Crick, Corrina Fear, Sharayne Robinson, Lisa Swift, Laure Gambardella, Johannes Bargehr, Daniel Ortmann, Stephanie E. Brown, Anna Osnato, Michael P. Murphy, Gareth Corbett, William T. H. Gelson, George F. Mells, Peter Humphreys, Susan E. Davies, Irum Amin, Paul Gibbs, Sanjay Sinha, Sarah A. Teichmann, Andrew J. Butler, Teik Choon See, Espen Melum, Christopher J. E. Watson, Kourosh Saeb-Parsy†, Ludovic Vallier*†

*Corresponding author. Email: fs347@cam.ac.uk (F.S.); lv225@cam.ac.uk (L.V.)
†These authors contributed equally to this work.

Published 19 February 2021, *Science* **371**, 839 (2021)
DOI: 10.1126/science.aaz6964

This PDF file includes:

Materials and Methods
Figs. S1 to S16
Tables S1 to S3
Captions for Movies S1 to S9
Captions for Data S1 to S3
References

Other Supplementary Material for this manuscript includes the following:
(available at science.sciencemag.org/content/371/6531/839/suppl/DC1)

Movies S1 to S6, S8, and S9 (.mp4)
Movie S7 (.mov)
Data S1 to S3 (.xlsx)

Other Supplementary Materials for this manuscript include the following:

Movies S1 to S9
Movie S1: Movie S1 Carrier1 T1.mp4
Movie S2: Movie S2 Carrier1 T2.mp4
Movie S3: Movie S3 Cells1 T1.mp4
Movie S4: Movie S4 Cells1 T2.mp4
Movie S5: Movie S5 MR 3D reconstruction Carrier.mp4
Movie S6: Movie S6 MR 3D reconstruction Cells.mp4
Movie S7: Movie S7 Z-stack KRT19(GREEN)-RFP(RED).avi
Movie S8: Movie S8 3D reconstruction KRT19(GREEN)-RFP(RED).mp4
Movie S9: Movie S9 3D rendering KRT19(GREEN)-RFP(RED).mp4

Data S1 to S3
Data S1: Data S1 Differentially Expressed Genes in Primary Cholangiocytes.xlsx
Data S2: Data S2 Differentially Expressed Genes in Pseudotime.xlsx
Data S3: Data S2 Differentially Expressed Genes between organoids and primary cholangiocytes.xlsx

Materials and Methods

Ethical approval

Gallbladder, bile duct, liver biopsy and bile samples were obtained from deceased organ donors (National Research Ethics Committee East of England – Cambridge South 15/EE/0152). Human livers retrieved for transplantation but subsequently declined were used for ex vivo administration of cholangiocytes (National Research Ethics Committee East of England – Cambridge East 14/EE/0137). All human tissue was used after obtaining informed consent for use in research.

Tissue collection

Gallbladder, bile duct, liver biopsies and bile were obtained under sterile conditions from deceased transplant organ donors as rapidly as possible after cessation of circulation. Tissue samples, and liver retrieved for transplantation but subsequently declined, were transferred to the laboratory at 4°C in University of Wisconsin (UW®) organ presentation solution.

Tissue dissociation

Resected tissue (gallbladder, extrahepatic ducts and liver) was transferred to the lab as described above and processed immediately after resection. Gallbladder and extrahepatic bile duct samples were drained of bile and the organ lumen was exposed through a longitudinal incision. Liver samples were divided into 1cm^2 cubes prior to processing. All samples were washed twice with warm PBS with $Ca^{2+}Mg^{2+}$ +EDTA (0.5mM), followed by enzymatic digestion with using Liberase (0.2 Wünsch/ml) in an incubated shaker at 37ºC and 200 RPM for 30 minutes. DNAse I (2000 U/ml) was added to the solution to prevent cell clumping and increase viability. Liver samples were dissociated further using the Miltenyi Biotec GentleMACS tissue dissociator and GentleMacs Tissue Dissociation C Tubes. For the gallbladder and extrahepatic duct samples, gentle mechanical scrapping of the lumen was adequate to release the epithelial cells following enzymatic digestion. All cell suspensions were filtered through 70um filters to remove debris and remaining tissue, washed with PBS containing 1% BSA (W/V) and centrifuged at 400g, for 5mins in a refrigerated centrifuge maintaining a temperature of 4ºC. The cells were resuspended in Miltenyi Biotec red blood cell (RBC) lysis and incubated for 10 minutes at room temperature (RT). The Miltenyi Biotec Debris Removal solution kit was used according to the manufacturer's instructions to remove remaining debris and dead cells. For liver samples, the resulting cell suspensions were centrifuged at 50g for 5 minutes (4ºC) to pellet the hepatocyte fraction, the supernatant was collected and cholangiocytes were isolated as described below.

Cell isolation

Following tissue dissociation to single cells, cholangiocytes were isolated with Magnetic Associated Cell Sorting (MACS) using the Miltenyi Biotech autoMACS Pro separator and CD326 (EpCAM) MicroBeads according to the manufacturer's instructions. The resulting cells were counted, centrifuged at 444g for 5 minutes, resuspended to a concentration of 1000 cells/ µL and stored on ice.

10x Single Cell Library Making Process

GEM-RTs (Gel-beads-in-emulsion which barcode the ploy adenylated mRNAs, followed by Reverse Transcription) were broken and Silane magnetic beads are used to purify first stand cDNA from the GEM-RT mixture and the cDNA was then amplified via PCR. Enzymatic fragmentation, end-repair and A-tailing were followed by size selection (using SPRISelect reagent). An adapter was ligated to the fragments and following a clean-up step, index PCR took place. After a further round of size selection with SRISelect, completed libraries were quantified, (Agilent Bioanalyser and qPCR) and diluted for running on an Illumina sequencing instrument (HS4000).

Processing and normalization of 10X data

The results from the sequencing runs were checked manually to confirm that the overall yield and quality were as expected. The data from the instrument were converted to fastq format, the input format required by the 10X software cellranger, and aligned using the human reference GRCh36-1.2.0 available from 10X. The dataset was augmented by integrating counts of a cluster of cholangiocytes from a published dataset (cluster 17 in MacParland SA et al, 2018) (25). Cells were annotated as part of different origins, these being primary tissue (PRI), untreated organoids (ORG), treated organoids (ORGT). Each origin comprises three regions: intrahepatic duct (IHD), common bile duct (CBD), gallbladder (GB). The number of cells in each origin and region are reported in **Figure S1C**. Genes with read counts > 0 in at least 3 cells from each batch in at least one origin were maintained for downstream analysis. Low quality cells were removed based on the percentage of UMI mapping to the mitochondrial genome and the number of genes detected by determining outliers (3 median-absolute-deviations) with the routine isOutlier in the package scater (26). Cholangiocytes were isolated by retaining cells expressing at least one of the biliary markers EPCAM, KRT7, KRT19 (with number of counts > 3). Normalization, identification of highly variable genes and cell cycle regression (regressing out the difference between the G2M and S phase scores) were performed with the Seurat package (27). We employed the routine fastMNN in scran for batch correction (28). Batch corrected samples are shown in **figure 2A**. Small clusters derived by applying the Louvain method for community detection and characterized by cells which were outliers in the percentage of UMI mapping to the mitochondrial genome and the number of genes detected were filtered out.

Analysis of normalized 10X data

The normalized data were clustered using the Louvain method in the Scanpy package (29) by selecting a resolution which generated 3 clusters and with 10 random initialisations. Similarity between Louvain clusters and origin annotations was assessed using the Adjusted Rand Index (ARI) and the Adjusted Mutual Information (AMI). Both measures lie in the interval [0,1], where a value close to 0 indicates random labelling and exactly 1 means that the two partitions are identical. The average value calculated on the different partitions obtained by random initializations was > 0.95 for both measures, indicating a high correspondence between origins and clusters (**Fig. S5A**). The same analysis performed on regions showed poor matching between regions and clusters, suggesting similarity in the transcriptional profile of cells located in different regions (**Fig. S5A-B**). Transcriptional similarity was quantified at origin and region resolution by estimating the connectivity of data manifold partitions within the partition-based graph abstraction (PAGA) framework. At the origin resolution, this analysis notably highlighted higher transcriptional similarity between treated organoids and primary tissue than between untreated organoids and primary tissue (**Fig. S9B**). Interestingly, at the region resolution we identified higher transcriptional similarity between adjacent locations in primary tissues, with intrahepatic duct and gallbladder having the lowest connectivity value. This association between connectivity and anatomical location, together with the similarity of cells located in different regions, suggested a gradual variation in the transcriptional profile of cells in primary tissue that could be represented as a pseudo-spatial dimension. In this view, we analyzed the primary tissue by applying two methods for pseudo-temporal (or pseudo-spatial) ordering: diffusion pseudo-time (30) and Monocle 2 (31). In Monocle 2 differential expression in pseudotime was calculated using the differential GeneTest routine. Both methods confirmed an association between transcriptional similarity and anatomical location, as highlighted by the density plot in **Figure S4B** and allowed the representation of regional markers along a pseudo-spatial dimension (**Fig. S4C**). Since the majority of cells had a diffusion pseudotime value >0.65 the density plot if figure **S4B** is shown in the range [0.65,0.9] to improve visualization and avoid overcrowding. We then analyzed each region individually in organoids (treated and untreated) and primary tissue to identify potential subpopulations of cells. Due to the relatively small sample sizes, we applied the clustering method SC3, whose high accuracy and robustness is derived combining multiple clustering solutions through a consensus approach (32). SC3 allows the user to pre-define the number of clusters. Because of the arbitrariness of this choice we varied the number of clusters between 1 and 10, calculated the stability of clusters across resolutions (SC3 stability index) and built a clustering tree showing how cells move as the clustering resolution is increased (package clustree), (33). As shown in **Figure S5C**, no stable sub-trees were formed within each region, indicating absence of stable clusters defining subpopulations of cells.

Regional markers and differentially expressed genes were identified by applying the Wilcoxon-Rank-Sum test (p-value<0.01, |log2 fold change| > 1) in Scanpy. Gene set, gene ontology and pathway enrichment were performed using the packages GSEA (34) and Enrichr (35).

Data availability

10X raw data (fastq files) have been deposited in the repository ArrayExpress with the accession number E-MTAB-8495

Organoid derivation and culture

A portion of the cells isolated for scRNAseq was cultured and propagated as organoids using our established methodology (11, 12). Cells were cultured under the same conditions irrespective of their region of origin.

Immunofluorescence, RNA extraction and Quantitative Real Time PCR

IF, RNA extraction and QPCR were performed as previously described (3, 16, 36, 37). A complete list of the primary and secondary antibodies used is provided in **table S2**. A complete list of the primers used is provided in **table S3**.

All QPCR data are presented as the median, interquartile range (IQR) and range (minimum to maximum) of four independent lines unless otherwise stated. Values are relative to the housekeeping gene Hydroxymethylbilane Synthase (HMBS).

All IF images were acquired using a Zeiss Axiovert 200M inverted microscope or a Zeiss LSM 700 confocal microscope. Imagej 1.48k software (Wayne Rasband, NIHR, USA, http://imagej.nih.gov/ij) was used for image processing. IF images are representative of 3 different experiments.

GGT activity

GGT activity was measured in triplicate using the MaxDiscovery™ gamma-Glutamyl Transferase (GGT) Enzymatic Assay Kit (Bioo scientific) based on the manufacturer's instructions. Error bars represent SD.

<u>Alkaline Phosphatase staining</u>

Alkaline phosphatase was carried out using the BCIP/NBT Color Development Substrate (5-bromo-4-chloro-3-indolyl-phosphate/nitro blue tetrazolium) (Promega) according to the manufacturer's instructions.

<u>Flow cytometry analyses</u>

Flow cytometry analyses were performed as previously described (11, 12, 28, 29).

<u>Bile acid treatment</u>

Organoids were incubated for 72 hours with 10μM CDA (Sigma, C9377-5G) in the presence or absence of 10μM Z-GS (Santa Cruz, sc-204414).

<u>Animal experiments</u>

All animal experiments were performed in accordance with UK Home Office regulations (UK Home Office Project License number PPL 70/8702). Immunodeficient NSG mice (NOD.Cg-Prkdcscid Il2rgtm1Wjl/SzJ), which lack B, T and NK lymphocytes, were bred in house, and food and water were available ad libitum before and after procedures. Male animals aged 4–8 weeks were used. Animals were assigned randomly to treatment and control groups. Experiments were performed blinded, and where this was not possible (e.g., due to performance of a surgical procedure), data were analysed blinded to the identity of the experimental groups. Littermate animals were used as controls.

<u>Cell delivery</u>

Cholangiocytes were delivered into the liver retrogradely through the extrahepatic biliary tree (14). In brief, a fine bore cannula was placed and secured in the gallbladder. To divert the infusion into the liver, the distal common bile duct was occluded with a clamp. The cells were infused through the cannula in the gallbladder in a total volume of 1μl/g of total body weight, at a maximum speed of 1μl/second.

<u>MDA administration</u>

Cholangiopathy was induced through intraperitoneal (IP) administration of 4,4′-methylene dianiline (MDA) on 3 occasions 7, 5, and 3 days prior to cell delivery at a concentration of 50 μg/g of total body weight. An additional dose of MDA was administered directly into the extrahepatic biliary tree prior to cell delivery as described above.

<u>Blood sample collection</u>

Blood was taken using a 23g needle directly from the inferior vena cava under terminal anesthesia at the time the animals were electively culled and transferred into 1.5ml Eppendorf tubes for further processing.

<u>Blood sample processing</u>

The blood samples were routinely processed by the University of Cambridge Core biochemical assay laboratory (CBAL). All of the sample analysis was performed on a Siemens Dimension EXL analyzer using reagents and assay protocols supplied by Siemens.

Tissue collection

Tissue for sectioning and staining was collected at the end of all animal experiments when the animals were culled, unless otherwise stated. The animals were culled due to due to animal welfare reasons (weight loss, jaundice and clinical deterioration) or electively 3 months after transplantation. Timepoints are indicated on the relevant Kaplan-Meier curves **(Fig. 3B; Fig. S13A).**

Cryosectioning

Excised tissue was fixed in 4% PFA, immersed in sucrose solution overnight, mounted in optimal cutting temperature (OCT) compound and stored at -80°C until sectioning. Sections were cut to a thickness of 6-10μm using a cryostat microtome and mounted on microscopy slides for further analysis.

Haematoxylin and Eosin (H&E) Staining

H&E staining was performed by the histology service of Addenbrooke's hospital or using Sigma-Aldrich reagents according to the manufacturer's instructions. Briefly, tissue sections were hydrated, treated with Meyer's Haematoxylin solution for 5 minutes (Sigma-Aldrich), washed with warm tap water for 15 minutes, placed in distilled water for 30-60 seconds and treated with eosin solution (Sigma-Aldrich) for 30-60 seconds. The sections were subsequently dehydrated and mounted using the Eukitt® quick-hardening mounting medium (Sigma-Aldrich).

Histology

Histology sections were reviewed by an independent histopathologist with a special interest in hepatobiliary histology (SD).

Quantification of transplanted cells in mouse liver

For each animal 3 random sections were analyzed, with different lobes being assessed. A total of 49,846 cells were analyzed, approximately 10,000 cells per animal.

MR imaging

Magnetic resonance cholangio-pancreatography was performed after sacrifice of the animals. MRCP was performed at 9.4T using a Bruker BioSpec 94/20 system (Bruker, Ettlingen, Germany). For higher signal to noise ratio to give improved visualisation of the biliary ducts a two-dimensional sequence was used with slightly varied parameters (24 spaced echoes at 11ms intervals to give an effective echo time of 110ms; repetition time 5741ms; matrix size of 256×256; field of view of 4.33×5.35cm2 yielding a planar resolution of 170×200μm2). Slices were acquired coronally through the liver and gall bladder with a thickness of 0.6mm. For this acquisition, a volume coil was used to reduce the impact of radiofrequency inhomogeneity.

To examine the biliary tree, images were prepared by maximum intensity projections. Structural imaging to rule out neoplastic growths was performed using a T1-weighted 3D FLASH (fast low-angle shot) sequence with a flip angle of 25°, repetition time of 14ms and an echo time of 7ms. The matrix was 512×256×256 with a field of view of 5.12×2.56×2.56cm3 for a final isotropic resolution of 100 µm.

Volume rendered images of the biliary tree were generated from source data using Osirix software. The region of interest was segmented from the remaining data manually.

The MRCP images were reviewed by 2 independent radiologists with a special interest in hepatobiliary radiology (EMG, SU).

Ex vivo normothermic perfusion of donor livers

The *metra* (OrganOx, Oxford, UK) normothermic liver perfusion device was used for ex vivo perfusion of human livers as previously described (20, 38). The machine, which is clinically used for preservation of livers for transplantation (20) enables prolonged automated organ preservation by perfusing it with ABO-blood group-compatible normothermic oxygenated blood. The perfusion device incorporates online blood gas measurement, as well as software-controlled algorithms to maintain pH, PO2 and PCO2 (within physiological limits), temperature and mean arterial pressure within physiological normal limits. In brief, the hepatic artery, portal vein, inferior vena cava and bile duct were cannulated, connected to the device and perfusion commenced.

Bile duct cannulation

Cannulation of the bile duct was achieved by inserting two 4 Fr sheaths into the common bile duct under fluoroscopy guidance, followed by cannulation of the left and right hepatic ducts and subsequently segment 3 and segment 5 ducts respectively, using two 2.7 Fr microcatheters via the sheaths. Peripheral placement of the microcatheters was confirmed by cholangiogram with small amount of ionic contrast medium. Cells were injected into segment 3 and carrier was injected into segment 5.

Cell delivery

RFP-expressing organoids were mechanically dissociated to a mixture of small clumps and single cells and approximately 10x106 RFP-expressing cells were administered in a peripheral duct of segment 3 with a distribution area of ~2cm^3, which was cannulated under fluoroscopic guidance to maximize cell delivery (see Bile duct cannulation section) (**Fig. S15B**). Carrier medium was delivered in a peripheral branch of segment 5 using the same technique and the organ was maintained on NMP for up to 100 hours.

Quantification of transplanted cells in human livers

3 human livers injected with RFP-labelled gallbladder organoids were analysed. Sections were obtained from the area of the distribution of the cells (~2cm^3). 5 sections per liver and a total of 4,463 cells were analysed.

Bile aspiration

Bile duct cannulation was performed as described in the relevant section. Following cannulation, 2 microfluidic catheters (CMA Microdialysis Catheter, Harvard Biosience Inc, USA) were placed into the respective segmental ducts using a guide wire exchange technique. The inner and outer shaft of the catheter and the inlet and outlet tubing are made of polyurethane and the membrane composed of polyarylethersulphone with a membrane pore size of 100kDa and outer diameter of 0.4mm. The inlet tubing for each catheter was connected to a portable battery driven

CMA 107 Microdialysis Pump (Harvard Biosience Inc, USA) and the pump was set to aspirate at a rate of 1µl/min.

Bile volume and pH measurements

Measurements were performed in n=3 different livers. A minimum of 2 repeat measurements were performed for each liver increasing to 3 where possible, as previously described (38). Bile volume was normalised over the volume of the bile ducts producing it, which corresponds to the volume of distribution of the cells or the carrier in the control arm. This was calculated using the volume of the contrast medium required to delineate these ducts on cholangiogram. Please note all catheters were primed prior to volume measurements.

Ultrasound imaging

The liver was imaged ex-vivo in a normothermic perfusion device using a Hitachi Aloka Arrieta V70 and a 10Mhz hand-held probe. Images were obtained in axial and sagittal planes and assessment of the portal vein, hepatic veins and their major branches was carried out. The intrahepatic bile ducts were also assessed, with particular attention to segment 3 where the organoids had been instilled, and a control area in segment 5 receiving carrier.

Statistical analysis

All statistical analyses were performed using GraphPad Prism 6. For small sample sizes where descriptive statistics are not appropriate, individual data points were plotted. For comparison between 2 mean values a 2-sided Student's t-test was used to calculate statistical significance. The normal distribution of our values was confirmed using the D'Agostino & Pearson omnibus normality test where appropriate. Variance between samples was tested using the Brown-Forsythe test. For comparing multiple groups to a reference group one-way ANOVA followed by Dunnett's test was used between groups with equal variance, while the Kruskal-Wallis test followed by Dunn's test was applied for groups with unequal variance. Survival was compared using log-rank (Mantel-Cox) tests. Where the number of replicates (n) is given this refers to organoid lines or number of different animals unless otherwise stated.

For animal experiments, group sizes were estimated based on previous study variance. Final animal group sizes were chosen to allow elective culling at different time point while maintaining n > 4 animals surviving past 30 days to ensure reproducibility. No statistical methods were used to calculate sample size. No formal randomization method was used to assign animals to study groups. However, littermate animals from a cage were randomly assigned to experimental or control groups by a technician not involved in the study. No animals were excluded from the analysis. Blinding was used for radiology imaging.

Supplementary Figure 1

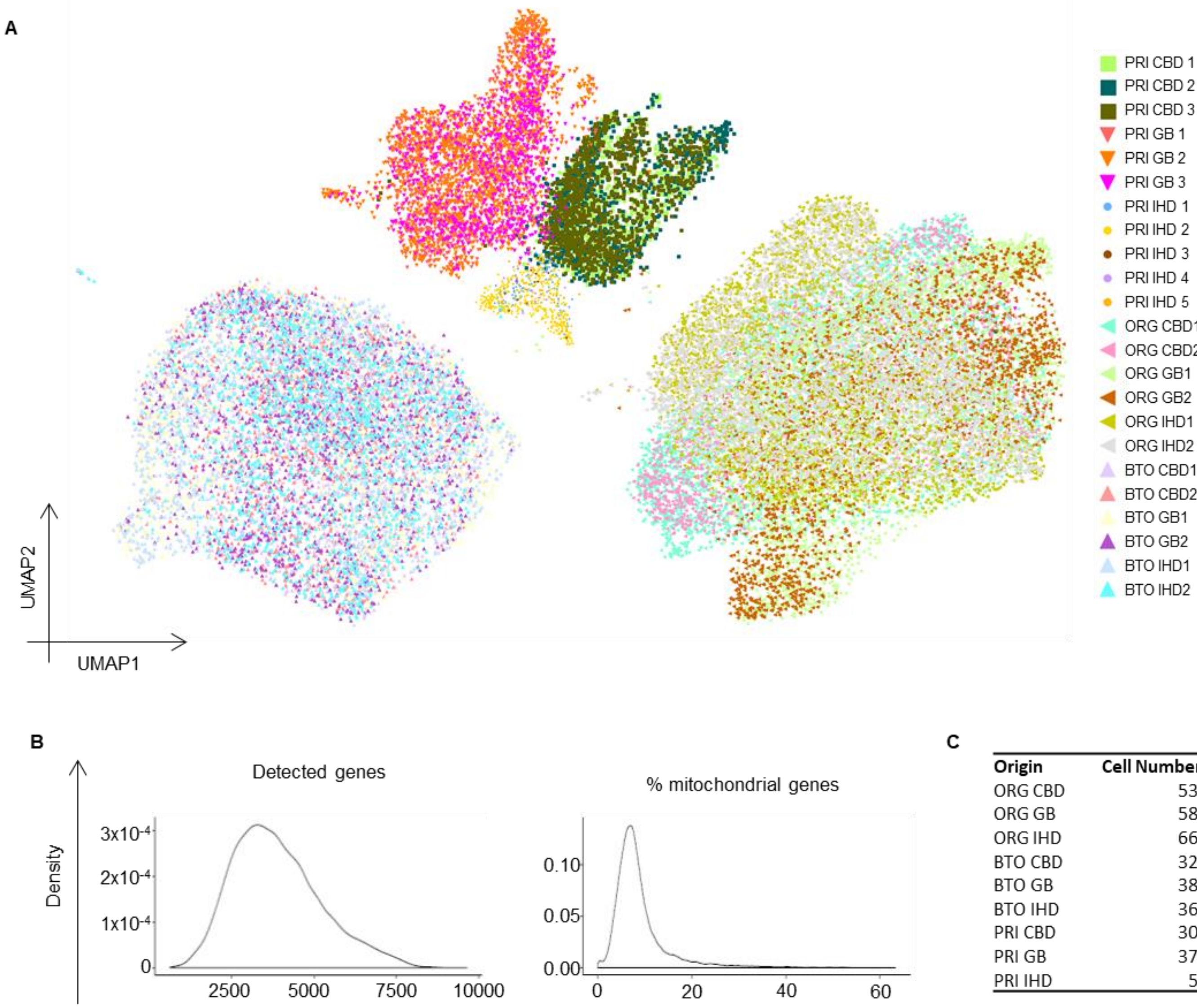

C

Origin	Cell Number
ORG CBD	5321
ORG GB	5859
ORG IHD	6641
BTO CBD	3224
BTO GB	3815
BTO IHD	3653
PRI CBD	3006
PRI GB	3702
PRI IHD	587

Fig. S1.

Characteristics and quality control of single cell RNA sequencing samples. (A) UMAP plot of all sequenced samples and 1 publicly available intrahepatic cholangiocyte dataset (PRI IHD 5; from MacParland SA et al, 2018, cluster 17). Each patient and cell line are distinguished by a unique color and marker combination. **(B)** Number of genes and percentage of mitochondrial genes detected per cell. **(C)** Number of cells isolated from each region PRI, Primary; IHD, IntraHepatic Ducts; CBD, Common Bile Duct; GB, Gallbladder; ORG, Organoids; BTO, Bile-treated organoids.

Supplementary Figure 2

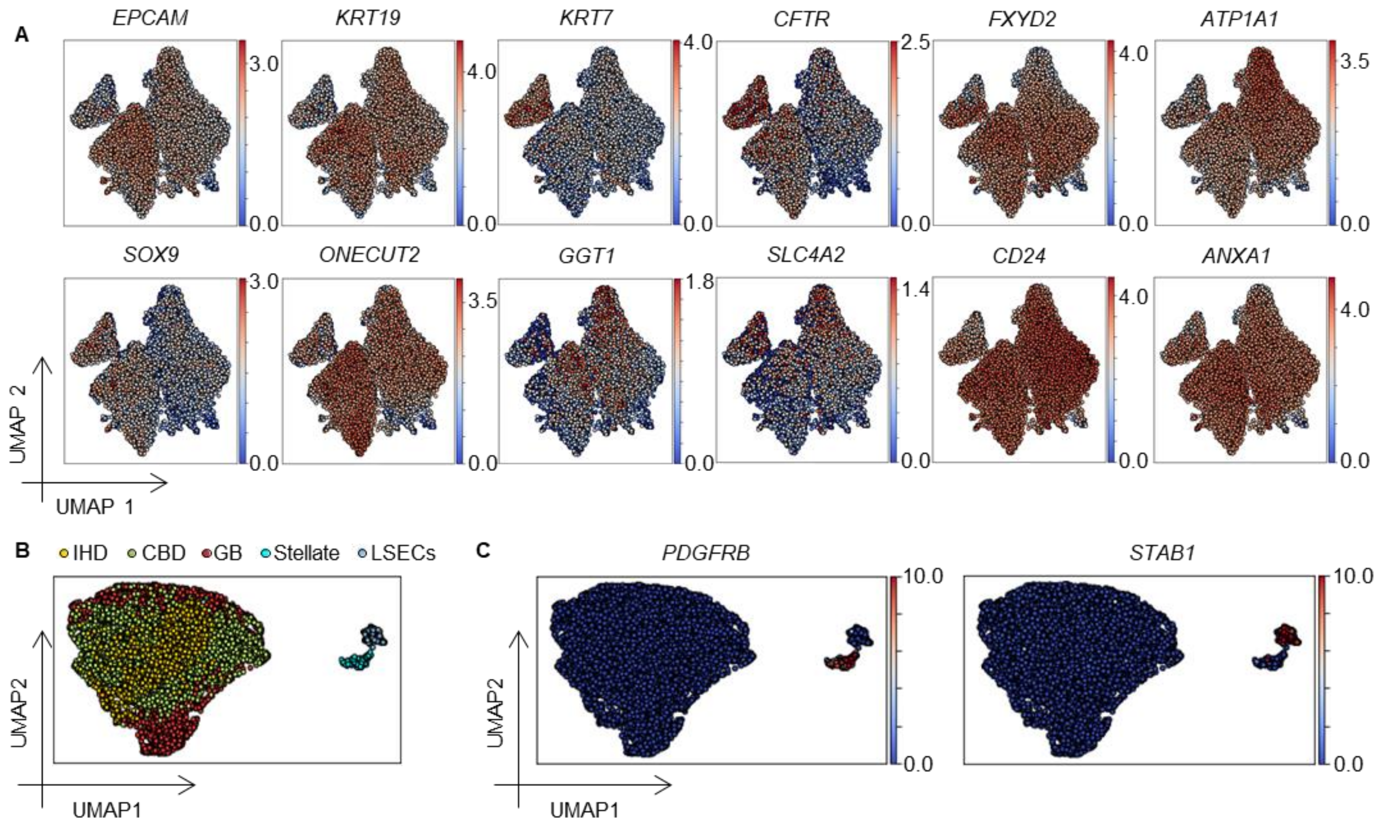

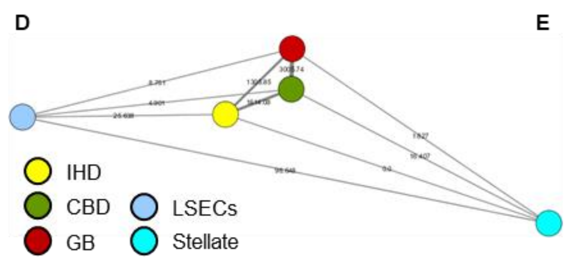

E

PAGA connectivity values

	LSECs	IHD	CBD	GB	Stellate
LSECs	N/A	0.25638	0.04901	0.08751	0.96648
IHD	0.25638	N/A	16.1408	13.0585	0
CBD	0.04901	16.1408	N/A	30.0574	0.16407
GB	0.08751	13.0585	30.0574	N/A	0.01627
Stellate	0.96648	0	0.16407	0.01627	N/A

Fig. S2.

Single cell RNA sequencing characterization of primary cholangiocytes. (A) UMAP plots demonstrating the expression of key cholangiocyte markers by the isolated cells, confirming their biliary identity. **(B)** UMAP plot of primary cholangiocytes compared to stellate and liver sinusoidal endothelial cells (LSECs) illustrating overlap between different region cholangiocytes when compared to a different cell type, which reflects a shared core biliary signature. **(C)** UMAP plots illustrating the expression of LSEC and stellate cell markers, confirming the cells' identity. **(D-E)** PAGA connectivity plot **(D)** and corresponding connectivity values **(E)** demonstrating a higher degree of transcriptional similarity between cholangiocytes from different regions compared to different cell types, confirming the shared core transcriptional signature of the cells. IHD, IntraHepatic Ducts; CBD, Common Bile Duct; GB, Gallbladder.

Supplementary Figure 3

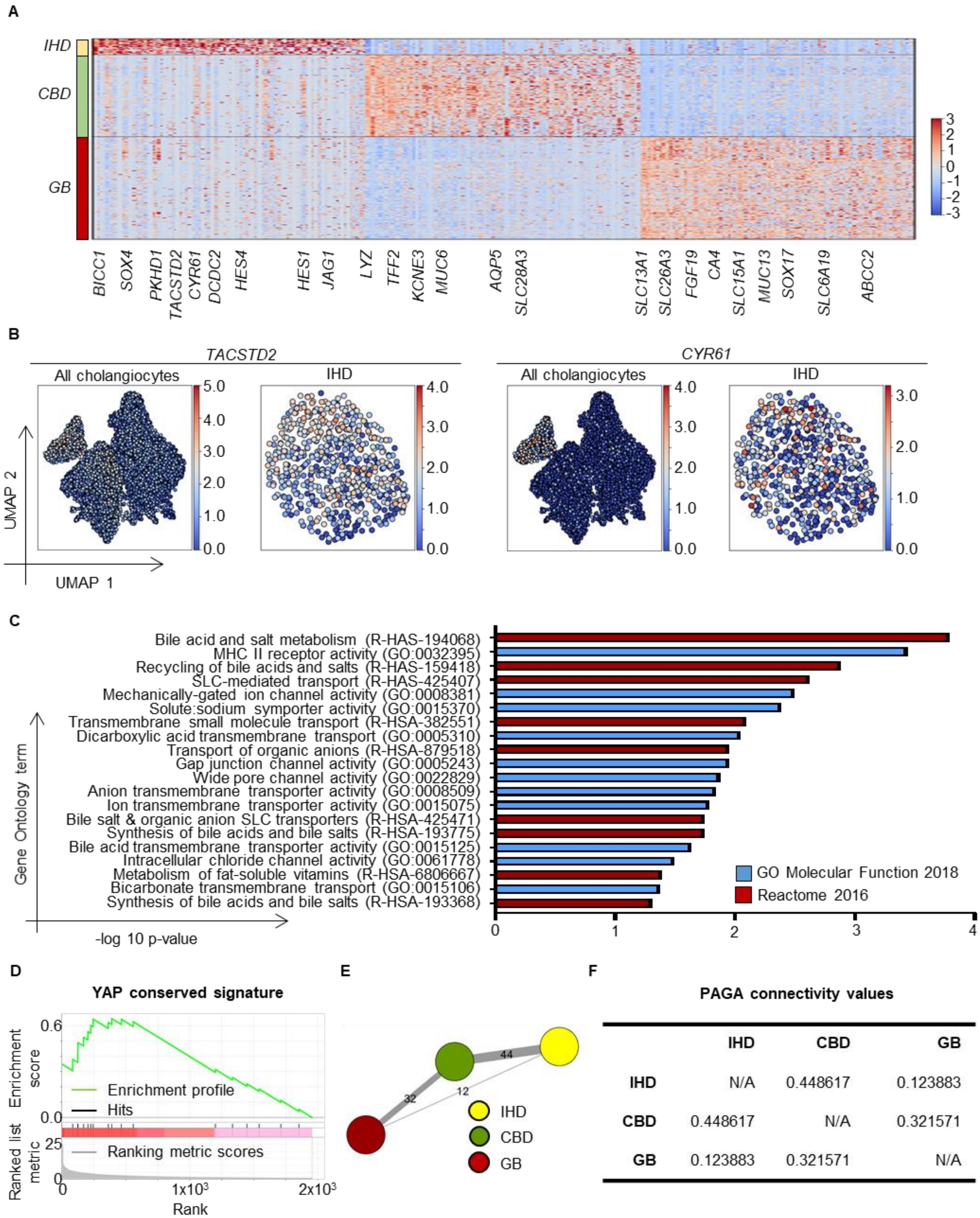

	IHD	CBD	GB
IHD	N/A	0.448617	0.123883
CBD	0.448617	N/A	0.321571
GB	0.123883	0.321571	N/A

Fig. S3.

Characterization of the transcriptional signature of cholangiocytes from different regions of the biliary tree. (A) Heatmap of top 100 Differentially Expressed Genes (DEGs) in cholangiocytes isolated from distinct regions of the biliary tree revealing transcriptional diversity in the primary biliary epithelium. IHD, IntraHepatic Ducts; CBD, Common Bile Duct; GB, Gallbladder (**Data S1**). **(B)** UMAP plots confirming the expression of previously described markers in IHDs. **(C)** Gene Ontology (GO) analysis on DEGs between biliary tree regions using EnrichR illustrating enrichment of cholangiocyte-to-niche interaction markers, such as bile processing and modifying genes. **(D)** Gene Set Enrichment Analyses on DEGs between biliary tree regions identifying differences in the expression of YAP target genes, $P<0.001$. **(E-F)** PAGA connectivity plot **(E)** and corresponding connectivity values **(F)** demonstrating a higher degree of transcriptional similarity between adjacent regions of the biliary tree. Connectivity values illustrated in **(E)** are multiplied by 100.

Supplementary Figure 4

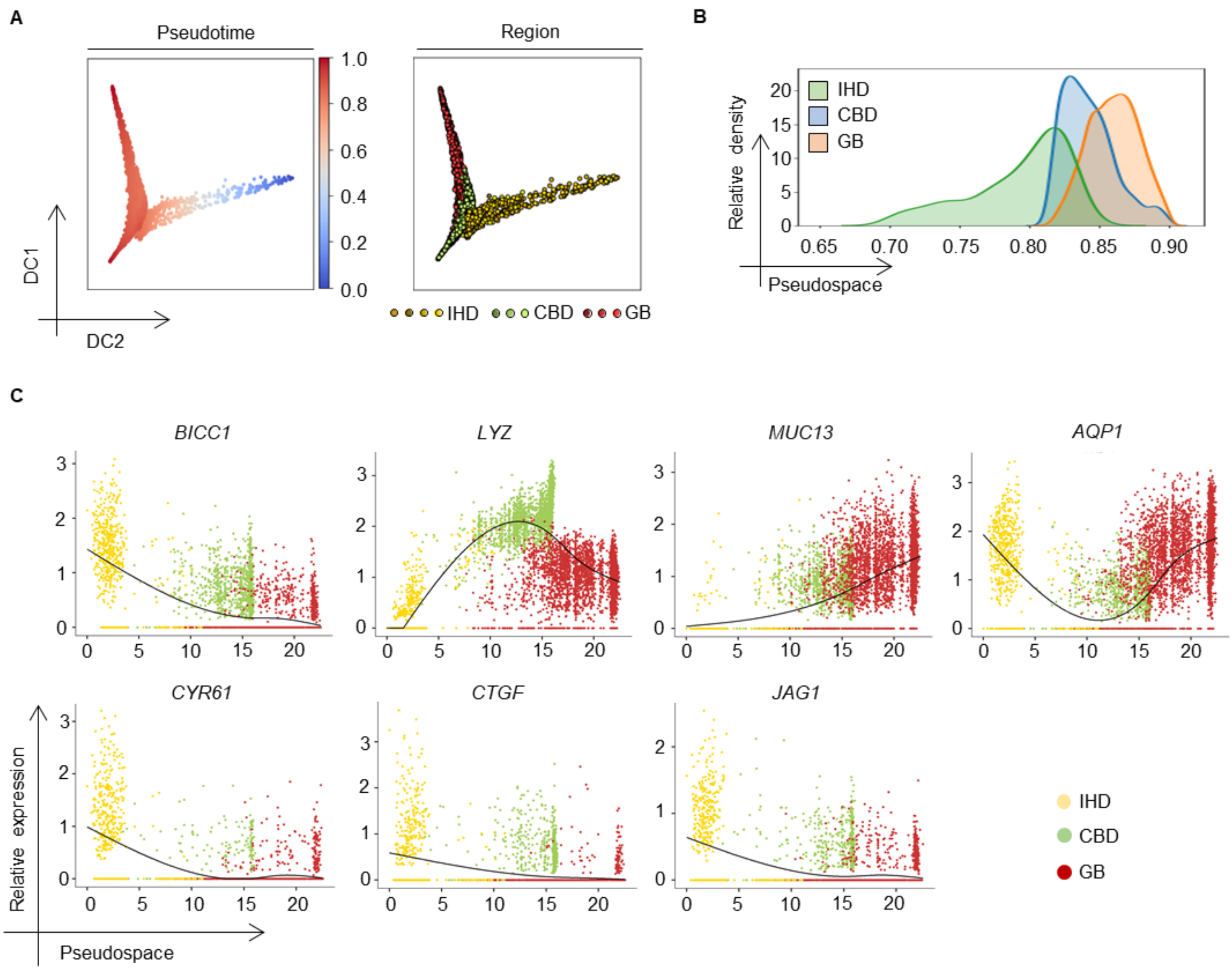

1

Fig. S4.

Pseudotime analysis of primary cholangiocytes. (A) Cell trajectory in pseudotime using Monocle; **(B)** Density plot of pseudo-time coordinates and **(C)** Gene expression in pseudotime of representative region markers indicating a gradual transition in transcriptional profile between cholangiocyte populations from adjacent regions. IHD: Intrahepatic Ducts, CBD: Common Bile Duct, GB: Gallbladder

Supplementary Figure 5

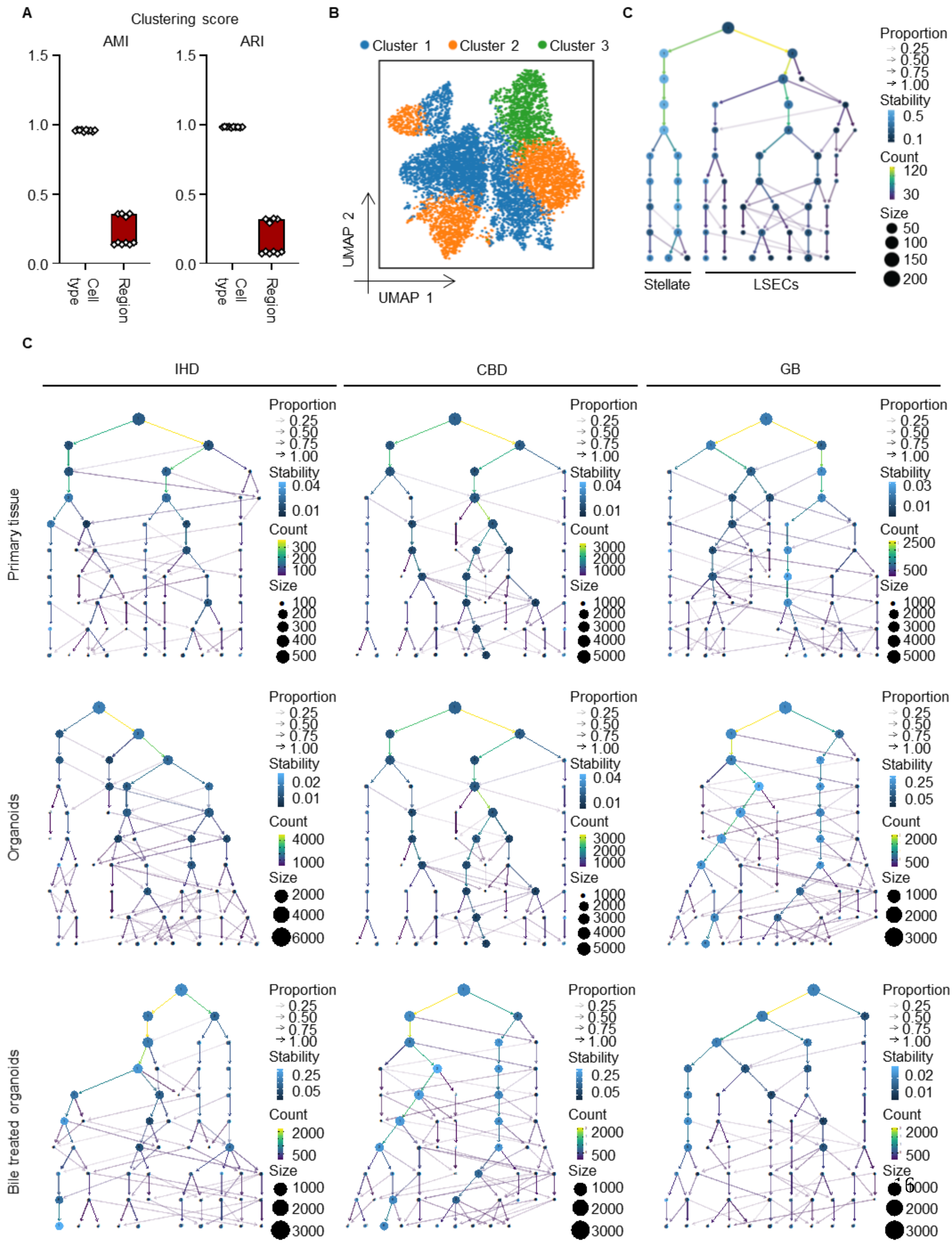

Fig. S5.

Characterization of cluster stability. (A) Adjusted Rand Index (ARI) and the Adjusted Mutual Information (AMI) confirming that primary cholangiocytes, organoids, and bile-treated organoids constitute distinct populations by illustrating a high correspondence between Louvain clusters and cell type (primary, organoids, bile-treated organoids) annotations (average value > 0.95 for both measures) vs. poor correspondence between Louvain clusters and region (intrahepatic ducts, common bile duct, gallbladder) annotations (average value<0.3 for both measures). **(B)** UMAP plot of Louvain clusters demonstrating poor matching between regions and clusters. The plot corresponds to the UMAP plot in **Fig. 1B** illustrating different regions. **(C-D)** Clustering trees derived from SC3 clusters by varying the pre-defined number of clusters k from 1 to 10 (see Methods) for a positive control comprising of stellate cells and LSECs **(C)** vs. cholangiocytes from different regions and corresponding cholangiocyte organoids **(D)**. Cluster stability across different clustering resolutions confirms the presence of different populations (stellate vs. LSECs) in the positive control **(C)**; while the absence of well-defined cholangiocyte subpopulations in each anatomical region or between organoids from different regions is demonstrated by the lack of stable clusters in **(D)**.

Supplementary Figure 6

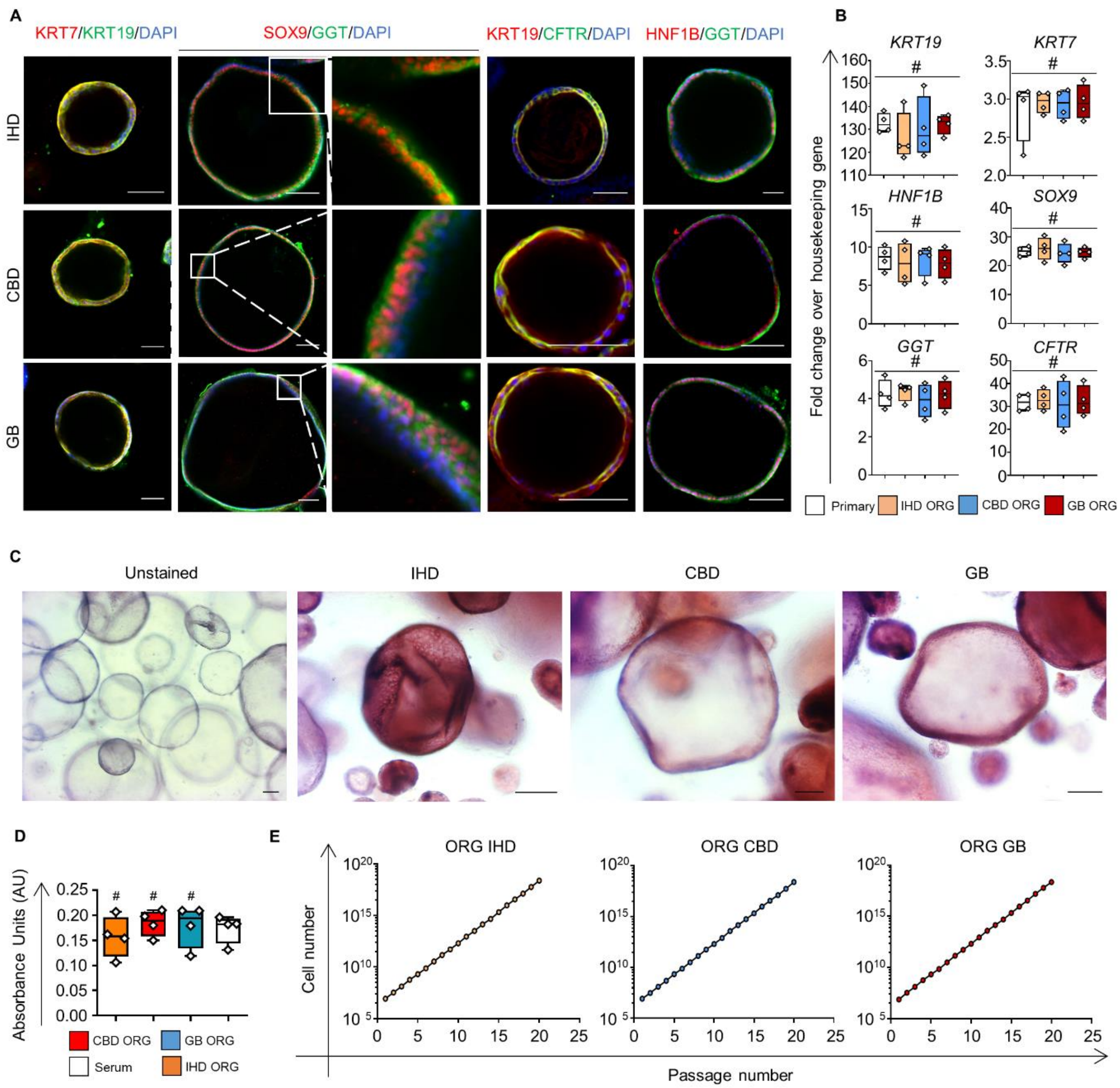

Fig. S6.

Characterization of cholangiocyte organoids from different regions of the biliary tree. (A) Immunofluorescence and **(B)** QPCR analysis of cholangiocyte organoids derived from different regions of the biliary tree demonstrating uniform expression of key biliary markers. n=4 samples per group; center line, median; box, interquartile range (IQR); whiskers, range; housekeeping gene, HMBS; #P>0.05#; scale bars, 50μm. **(C-D)** Organoids from different regions demonstrate Alkaline Phosphatase (ALP) **(C)** and GGT (Gamma-glutamyltransferase) **(D)** function. Scale bars, 100μm. **(E)** Growth curves illustrating comparable expansion potential between organoids from different regions. #, P>0.05. IHD, IntraHepatic Ducts; CBD, Common Bile Duct; GB, Gallbladder; ORG, Organoids; Primary, Primary CBD cholangiocytes.

Supplementary Figure 7

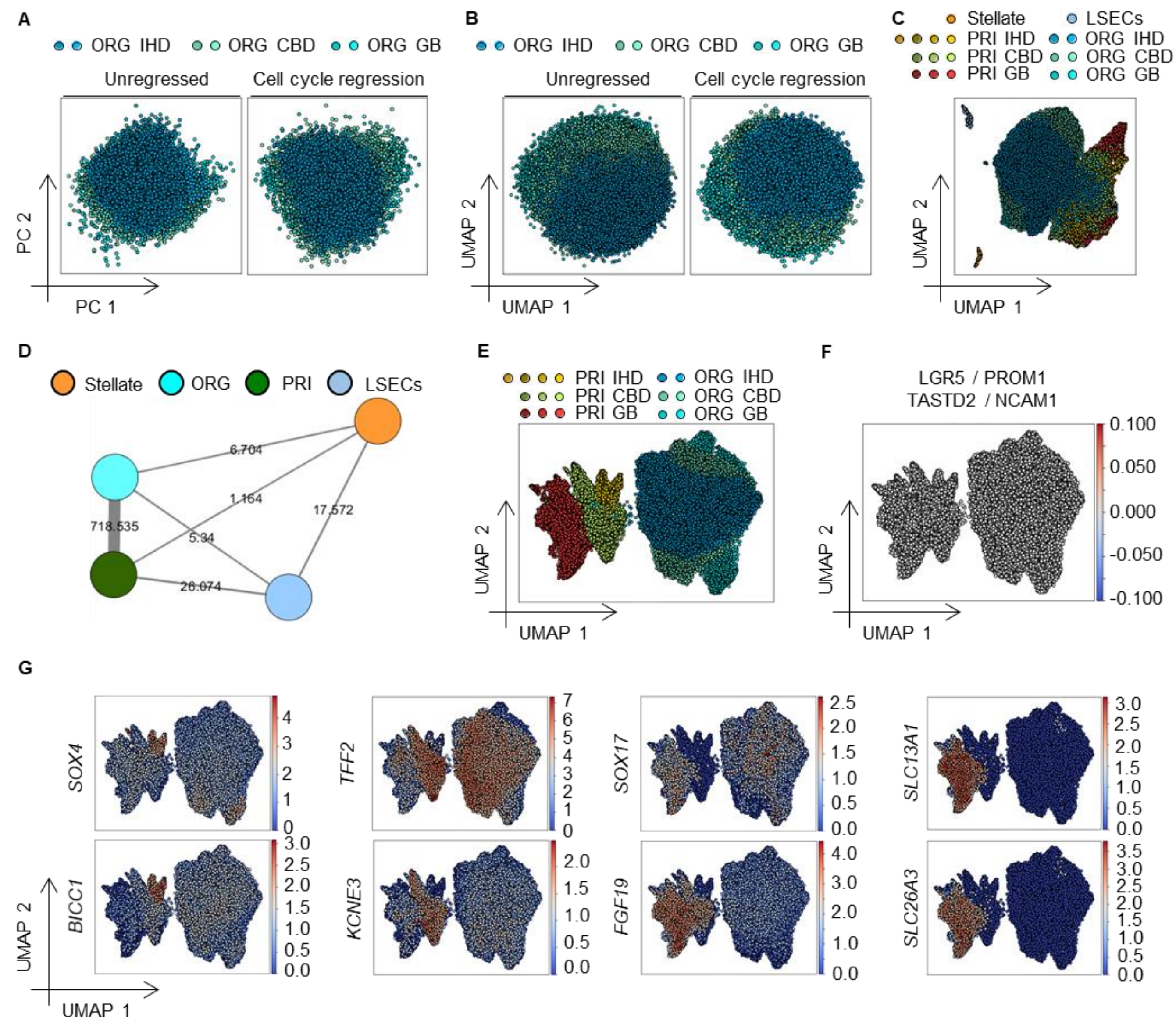

Fig. S7.

Single-cell RNA sequencing characterization of cholangiocyte organoids from different regions of the biliary tree. (A) PCA (unregressed, 24.8%; cell cycle regression, 21.8% of variance) and **(B)** UMAP representation demonstrating overlap in the transcriptional profile of different region organoids before and after cell cycle regression, confirming that cell cycle genes are not responsible for these similarities. **(C)** UMAP plot demonstrating that organoids and primary cholangiocytes irrespective of region occupy adjacent and overlapping spaces when compared to different cell types, illustrating a shared cholangiocyte transcriptional signature between biliary cells in vivo and in vitro. **(D)** PAGA connectivity plot demonstrating a higher degree of transcriptional similarity between cholangiocytes in vivo (PRI, Primary) and in vitro (ORG, organoids) compared to different cell types, confirming the shared core transcriptional signature of the cells. Respective connectivity values multiplied by 100 are illustrated on the plot. IHD, IntraHepatic Ducts; CBD, Common Bile Duct; GB, Gallbladder; LSECs, Liver Sinusoidal Endothelial Cells. **(E)** UMAP representation following regression of cell cycle genes illustrating that the similarities between cholangiocyte organoids are preserved despite cell-cycle regression and therefore they are not attributable to a common 'proliferation' signature. **(F)** UMAP representation of cells co-expressing somatic stem cell markers (normalized expression>1), illustrating that similarities between organoids are not attributable to a common 'stem cell' signature. **(G)** UMAP representation of normalized gene expression values showing that organoids lose differences in the expression of region marks in culture.

Supplementary Figure 8

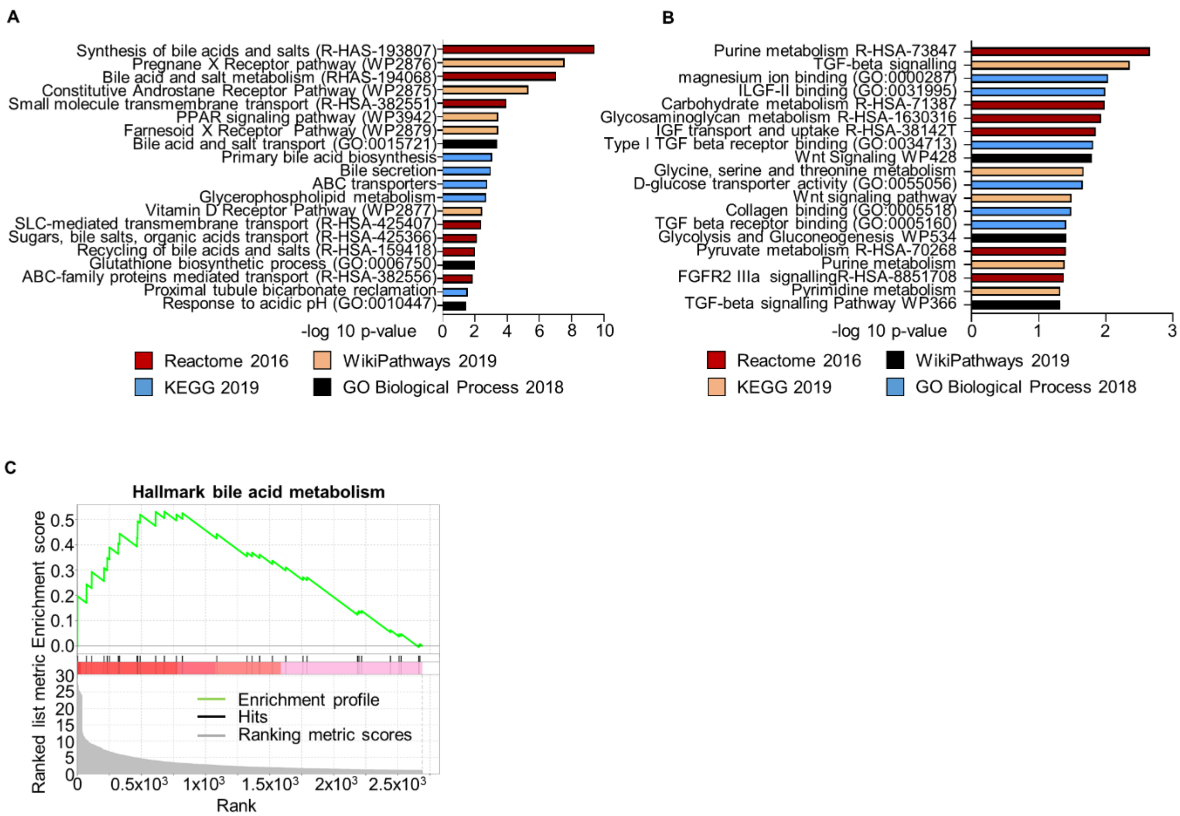

Fig. S8.

Gene ontology (GO) analyses on cholangiocyte organoids. (A-B) GO analysis on differentially expressed genes between primary cholangiocytes and organoids using EnrichR demonstrating that genes upregulated in primary tissue **(A)** are related to cholangiocyte-to-niche interaction, such as bile processing genes; while genes upregulated in organoids **(B)** reflect adaptation to cell culture conditions such as insulin, pyruvate and cytokine processing genes. **(C)** Gene Set Enrichment Analyses on DEGs between primary cells and organoids identifying differences in the expression of bile acid processing genes, P= 0.035. IHD, IntraHepatic Ducts; CBD, Common Bile Duct; GB, Gallbladder; ORG, Organoids.

Supplementary Figure 9

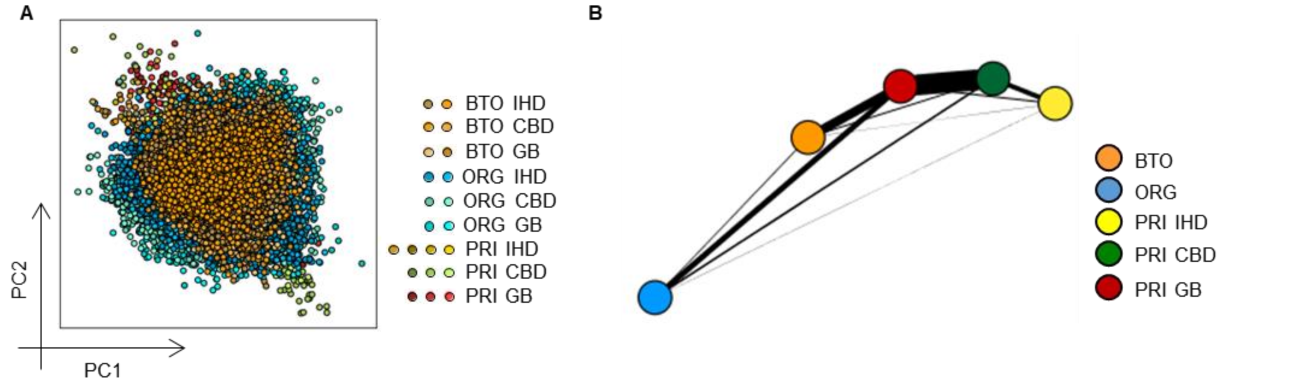

C

PAGA connectivity values

	ORG	BTO	PRI IHD	PRI CBD	PRI GB
ORG	N/A	0.001518	0.000138	0.003026	0.008304
BTO	0.001518	N/A	0.000215	0.001987	0.013333
PRI IHD	0.000138	0.000215	N/A	0.006934	0.002236
PRI CBD	0.003026	0.001987	0.006934	N/A	0.329157
PRI GB	0.008304	0.013333	0.002236	0.329157	N/A

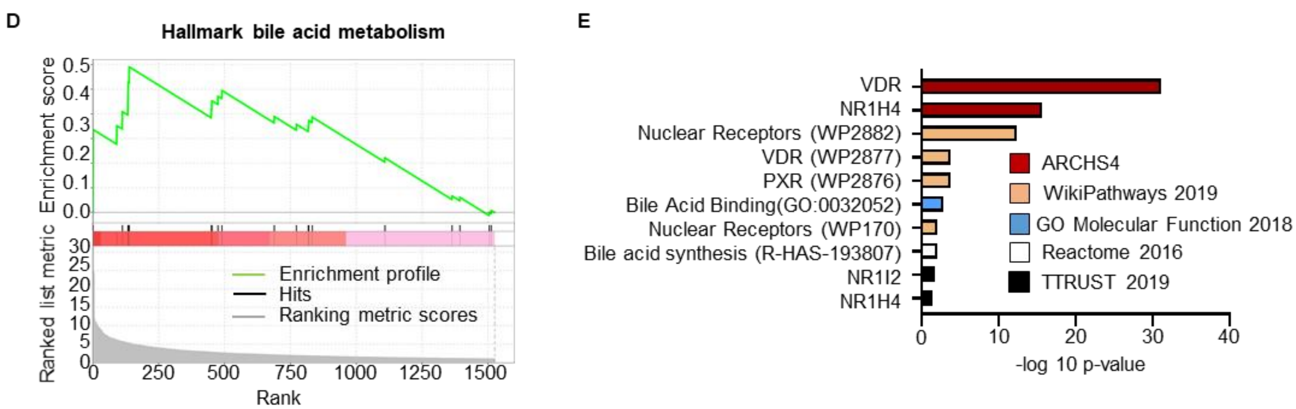

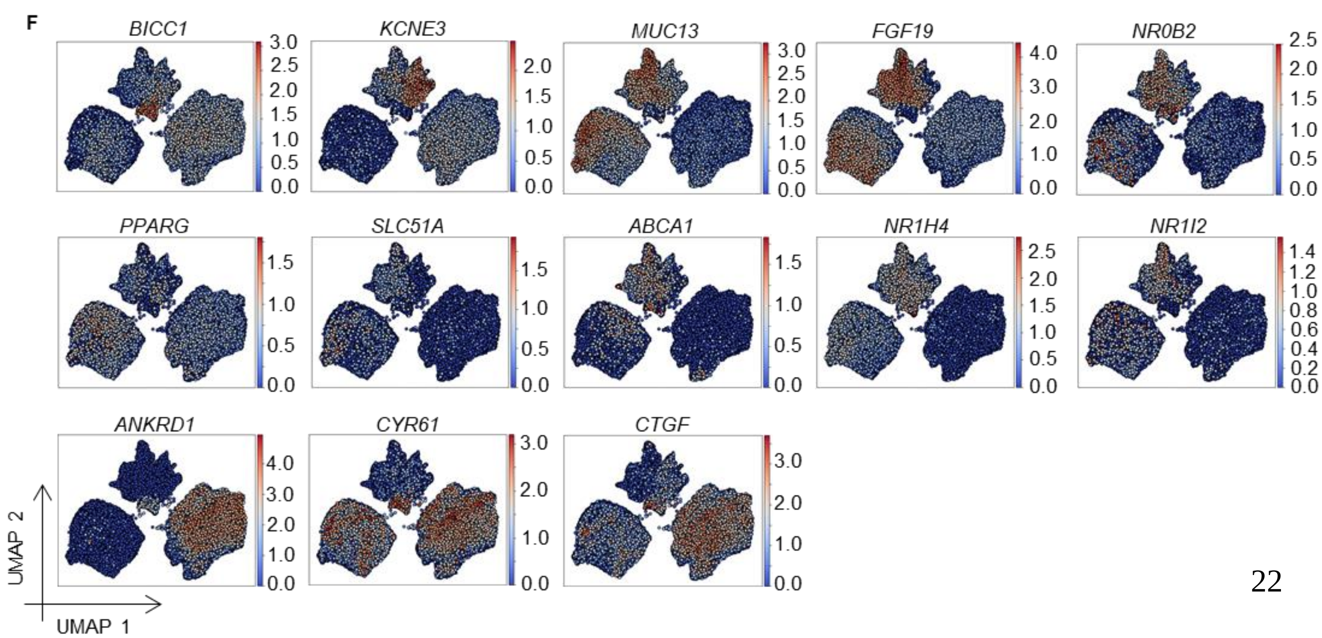

Fig. S9.

Characterization of bile-treated organoids. (A) PCA analysis (16.8% of variance) showing overlap between organoids, primary cholangiocytes and bile-treated organoids irrespective of region suggesting a shared core transcriptional profile between all cells. **(B)** PAGA connectivity plot demonstrating that bile-treated organoids (BTO) shift their transcriptional profile towards primary gallbladder cholangiocytes. **(C)** Connectivity values corresponding to the PAGA connectivity plot in panel **(B)** IHD, IntraHepatic Ducts; CBD, Common Bile Duct; GB, Gallbladder; ORG, Organoids; BTO, Bile-treated organoids; PRI, Primary. **(D-E)** GSEA **(D)** and GO analysis using EnrichR **(E)** on differentially expressed genes in organoids before and after treatment with bile showing enrichment in bile processing genes and in particular bile acid nuclear receptors and their downstream targets. P=0.012. **(F)** UMAP representation of normalized gene expression values illustrating upregulation of gallbladder markers and bile acid downstream targets following treatment of organoids with gallbladder bile.

Supplementary Figure 10

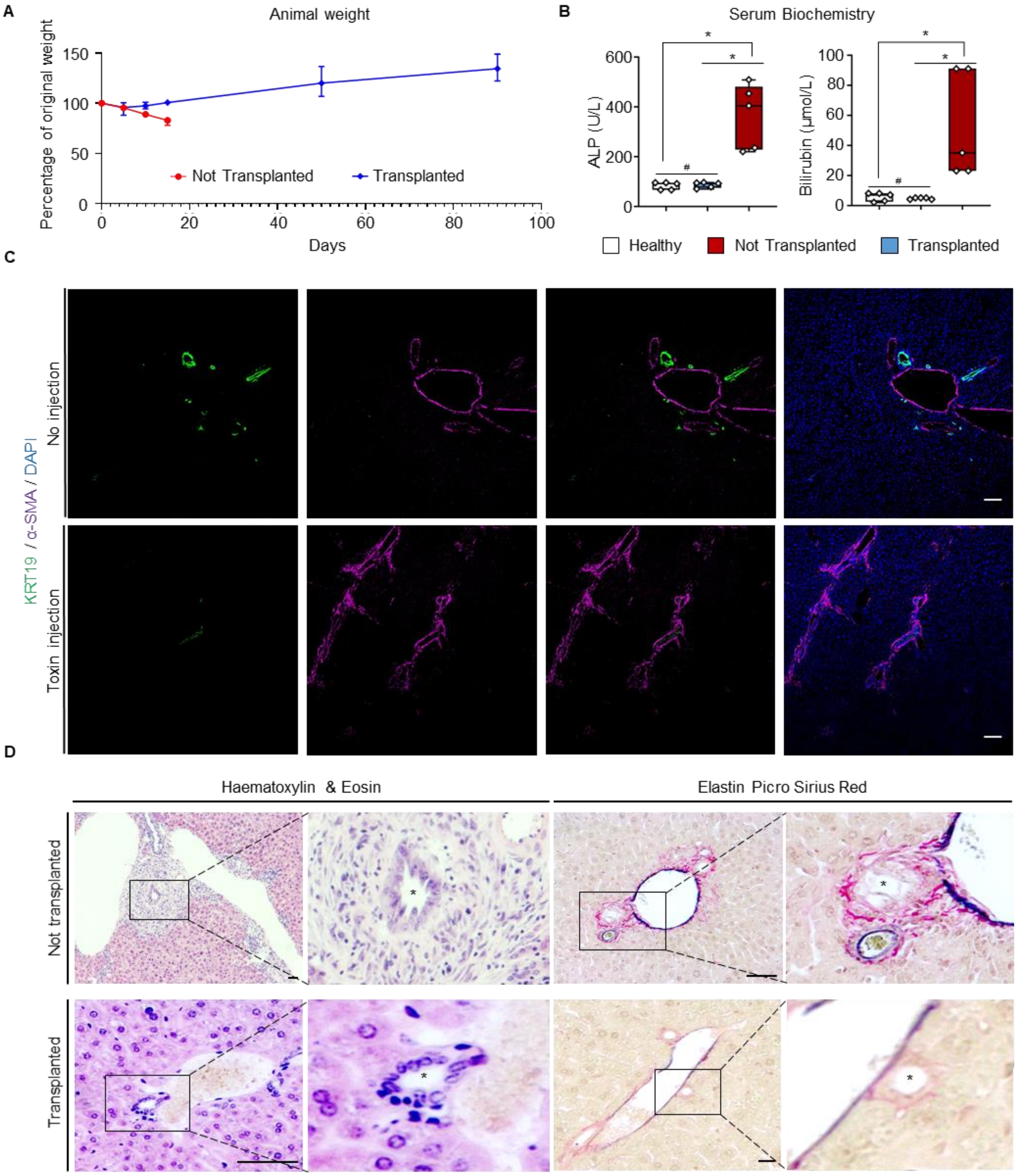

Fig. S10.

Gallbladder organoids rescue an acute cholangiopathy mouse model following transplantation. (A) Weight curve of animals treated with MDA (not transplanted) vs. animals injected with organoids following toxin treatment, demonstrating that injected animals recover and gain weight; n=5 animals in each arm. **(B)** Serum biochemistry demonstrating resolution of cholestasis following organoid injection; *P<0.05, #P>0.05, Kruskal-Wallis test. **(C)** Immunofluorescence images of MDA treated animals not transplanted with cells (toxin injection) vs. untreated controls (no injection) illustrating biliary injury following MDA administration. The images are complementary to **Fig. 3D**. **(D)** Histology (Heamatoxylin & Eosin and Elastic Picro Sirius Red) illustrating resolution of cholangiopathy following organoid injection. Asterisks: Bile ducts.

Supplementary Figure 11

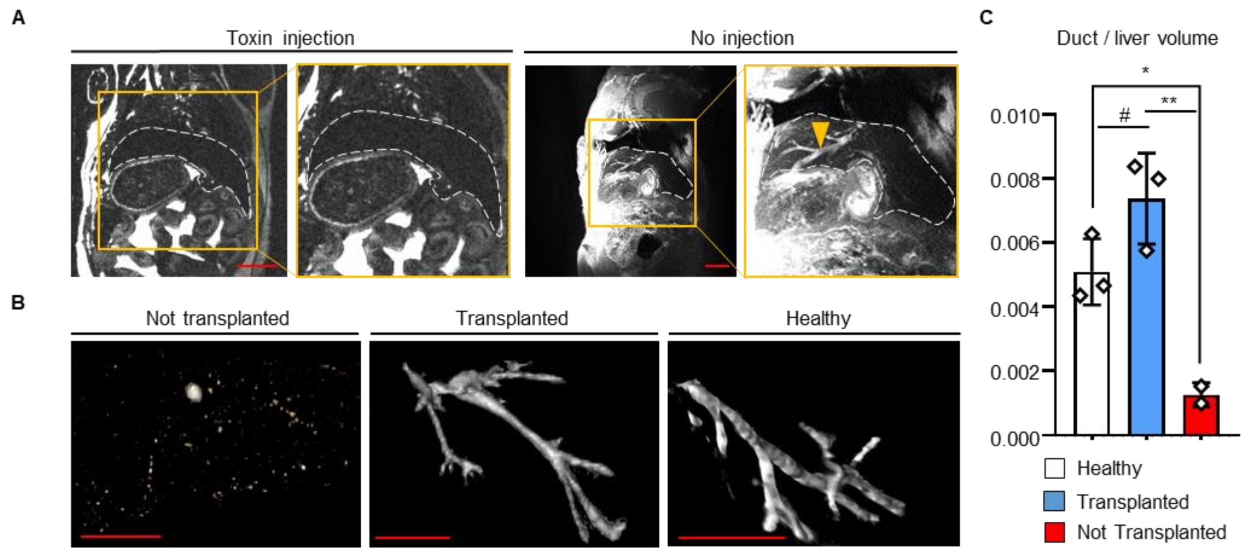

Fig. S11.

Gallbladder organoids regenerate the biliary tree of an acute cholangiopathy mouse model following transplantation. (A) Magnetic Resonance Cholangiopancreatography (MRCP) demonstrating biliary injury with loss of bile duct signal (white), immediately after toxin injection. The white dashed line outlines the liver margins. The image is complementary to **Fig. 3C.** Scale bars, 5mm. **(B)** 3D reconstruction of MRCP images demonstrating biliary injury with loss of bile duct signal in MDA-treated animals receiving carrier (not transplanted); vs. duct reconstruction in MDA-treated animals receiving organoid injections; vs. healthy animals. Scale bars, 5mm. **(C)** Quantification of bile duct signal on MRCP normalized over total liver volume in not transplanted vs. transplanted vs. healthy animals, demonstrating resolution of cholangiopathy following organoid injection; #, $P>0.05$; *, $P<0.05$; **, $P<0.01$; one-way ANOVA.

Supplementary Figure 12

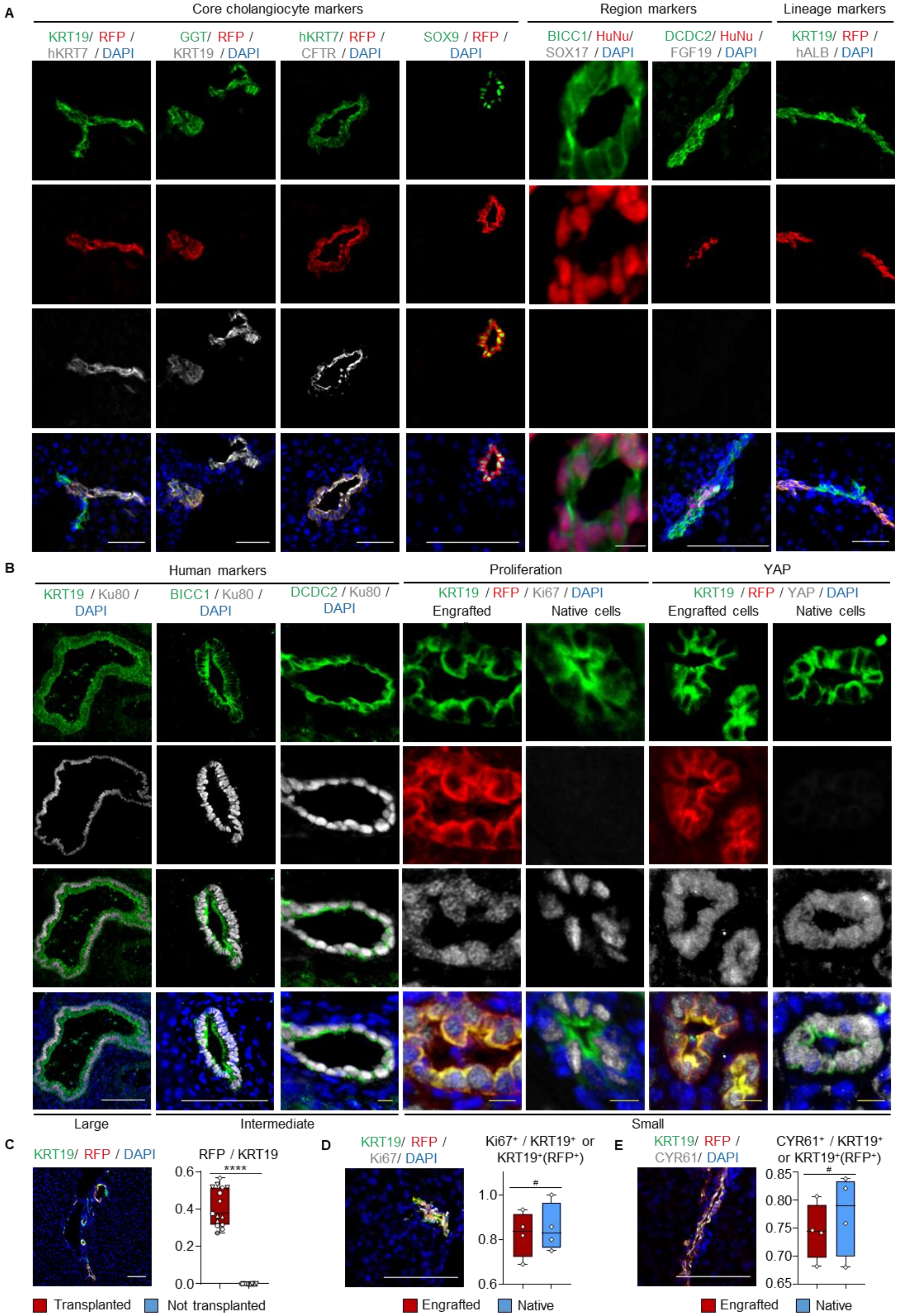

Fig. S12.

Gallbladder organoids regenerate the biliary epithelium of an acute cholangiopathy mouse model following transplantation. (A-B) Immunofluorescence analysis demonstrating engraftment, expression of key biliary markers, loss of gallbladder markers, expression of intrahepatic markers, absence of markers of other hepatic lineages **(A)**; and expression of human specific markers, proliferation markers and active YAP **(B)** in human Red Fluorescent Protein (RFP) expressing cells following transplantation in immunocompromised mice with cholangiopathy. Scale bars; **(A),** 50µm; **(B)**, 50µm (yellow), 100µm (white). The images are complementary to **Fig. 3**. **(C)** Quantification of human gallbladder-derived RFP-expressing cells in the bile ducts of transplanted vs. not transplanted animals; ** $P<0.01$; Mann-Whitney test. The data corresponds to 5 different animals and 3 random sections per animal. Each section is represented by a data point, while each animal is represented by a different symbol. **(D-E)** Quantification of the ratio of cells expressing proliferation markers (Ki67, **D**) and YAP downstream targets (CYR61, **E**) in ducts regenerated from engrafted human RFP-expressing cells vs. native mouse bile ducts in the same animals; # $P>0.05$; Mann-Whitney test.

Supplementary Figure 13

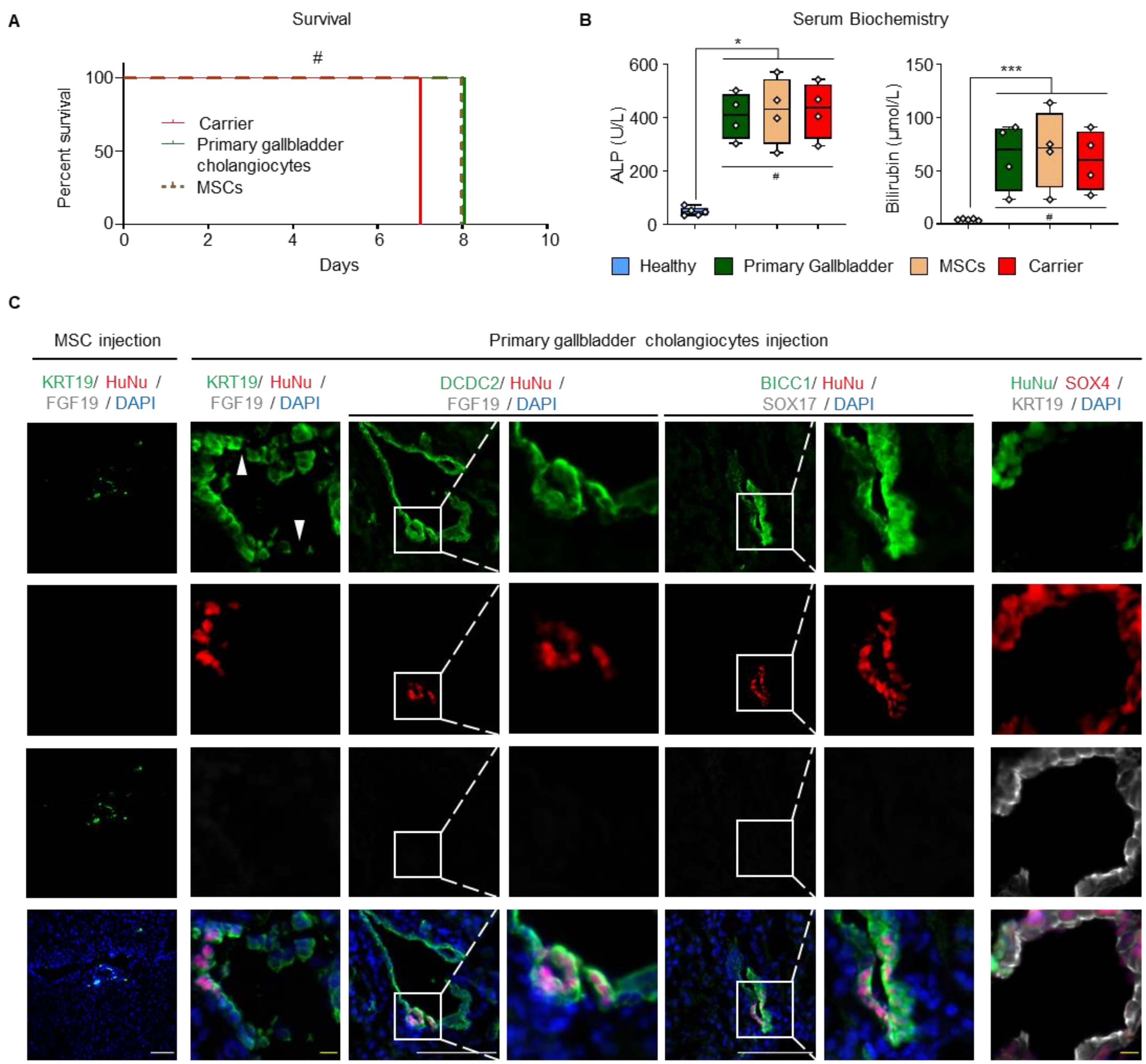

Fig. S13.

Primary human cholangiocytes and mesenchymal stem cells fail to rescue mice with acute cholangiopathy following transplantation. (A) Kaplan-Meier curve of mice with MDA-induced cholangiopathy receiving directly isolated human primary gallbladder cholangiocytes and human mesenchymal stem cells (MSCs) vs. carrier medium (carrier) demonstrating no statistically significant difference in survival between the three groups; $P>0.05$, log-rank test. **(B)** Serum biochemistry at the end of the experiment demonstrating persistent cholestasis in animals receiving primary gallbladder cholangiocytes, MSCs or carrier medium compared to healthy controls; *$P<0.05$, ***$P<0.001$, #$P>0.05$, one-way ANOVA. **(C)** Staining for human markers following cell transplantation reveals lack of engraftment of MSCs; while primary gallbladder cholangiocytes exhibit low level engraftment, which was not adequate to repair the damaged bile duct epithelium (white arrowheads). Engrafted primary gallbladder cholangiocytes lose gallbladder markers and upregulate intrahepatic markers. Scale bars; white, 100μm; yellow, 10 μm.

Supplementary Figure 14

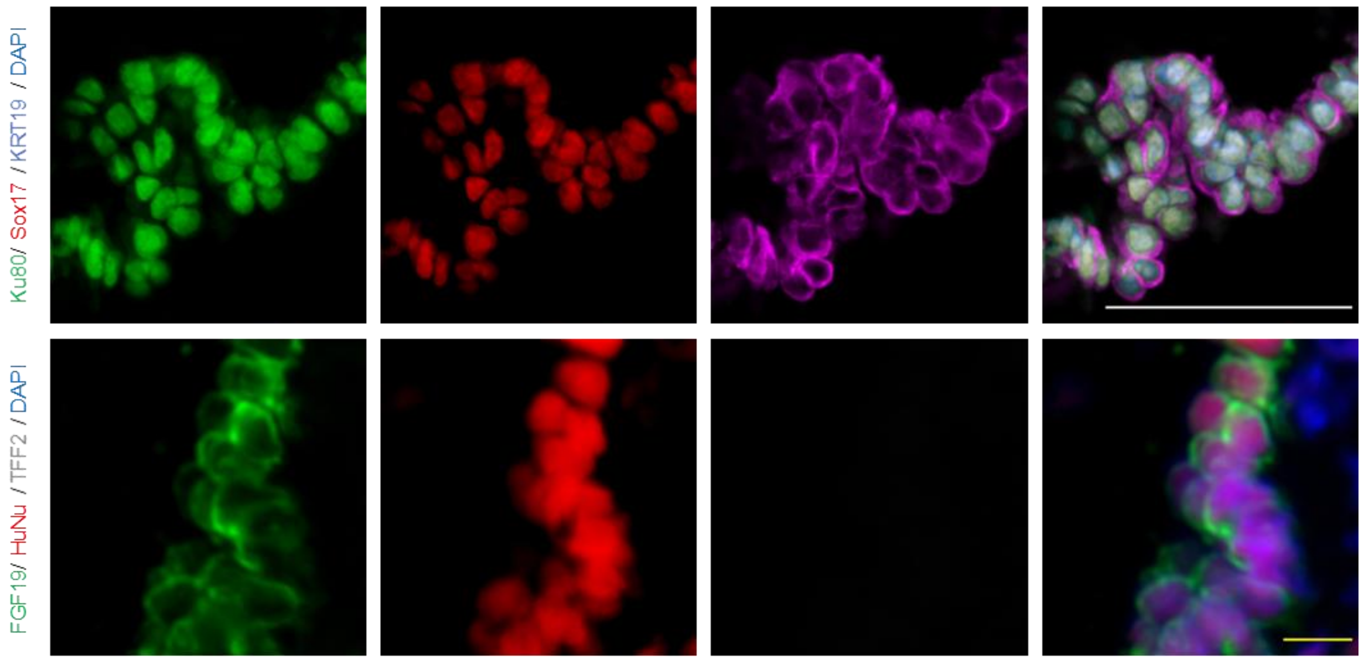

Fig. S14.

Transplantation of human common bile duct organoids in mouse gallbladder. Immunofluorescence analysis demonstrating expression of gallbladder markers and loss of common bile duct markers following transplantation of cholangiocyte organoids derived from human common bile duct in the gallbladder of immunocompromised mice. Scale bars; white, 100µm; yellow, 10µm.

1 **Supplementary Figure 15**

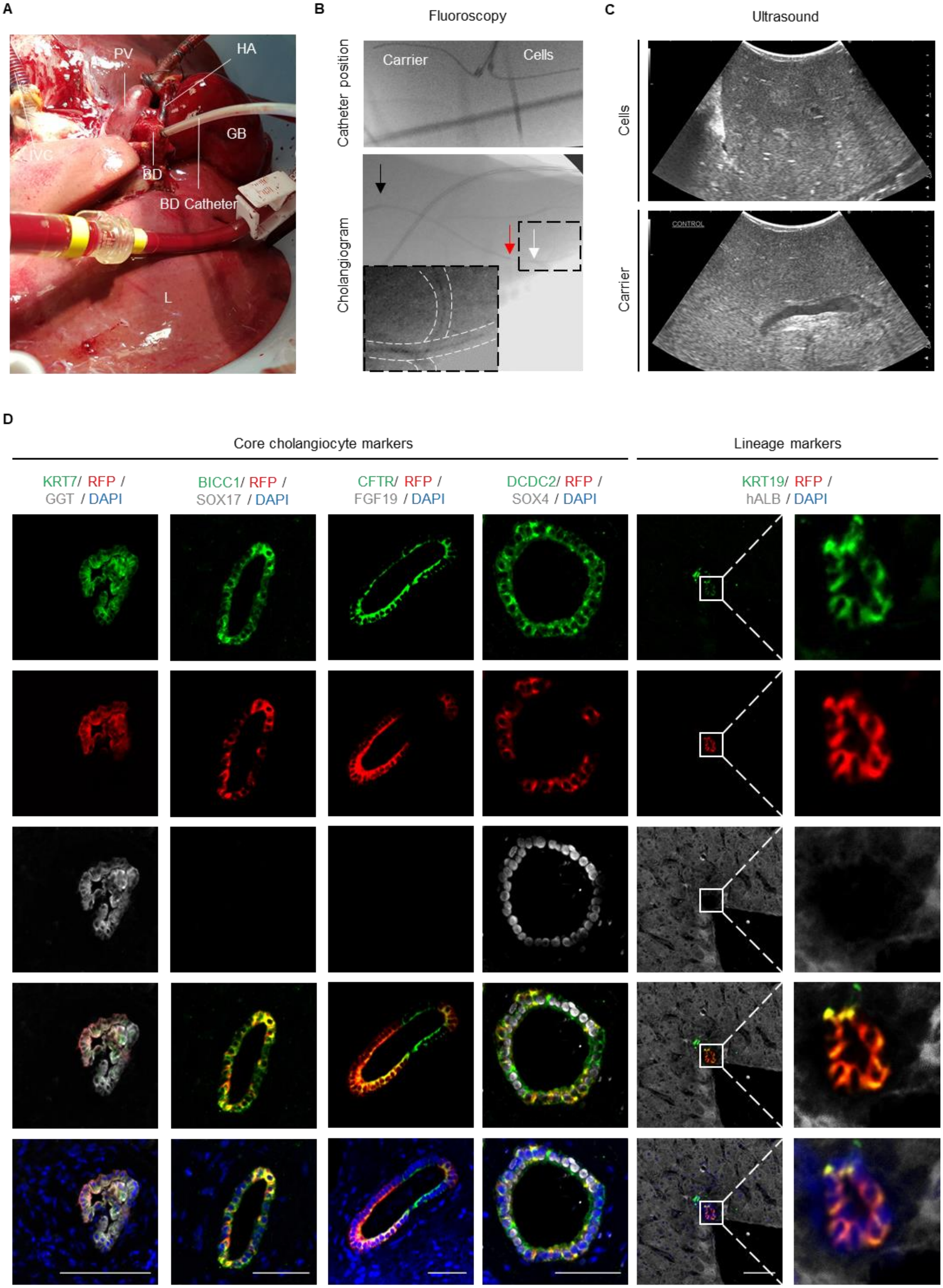

Fig. S15.

Administration of gallbladder organoids in human livers receiving Normothermic Perfusion (NMP). (A) Photograph of a human liver on NMP demonstrating anatomical landmarks, as well as the bile duct catheter used for administration of the Red Fluorescent Protein (RFP) expressing organoids. PV, portal vein; IVC, inferior vena cava; HA, hepatic artery; BD, Bile duct; GB, gallbladder; L, Liver. **(B)** Fluoroscopic images of peripheral duct cannulation. The position of the biliary catheters used for the injection of cells or carrier in the peripheral ducts of liver segments 3 and 5 respectively is shown in the top image. A cholangiogram of segment 3 following catheter placement, illustrating the peripheral position of the catheter and the area of distribution of injected the cells is shown in the bottom image. A magnified and contrast enhanced image is provided in the insert. Black arrow, sheath; red arrow, catheter tip; white arrow, cholangiogram. **(C)** Ultrasound imaging of the injected area of the liver revealing no duct dilation or any other abnormality at the end of the experiment. **(D)** Immunofluorescence analysis demonstrating engraftment, expression of key biliary markers, loss of gallbladder markers, expression of intrahepatic markers and loss of markers of other lineages in human Red Fluorescent Protein (RFP) expressing cells following transplantation in NMP human livers. Scale bars, 50μm. The images are complementary to **Fig. 4**.

Supplementary Figure 16

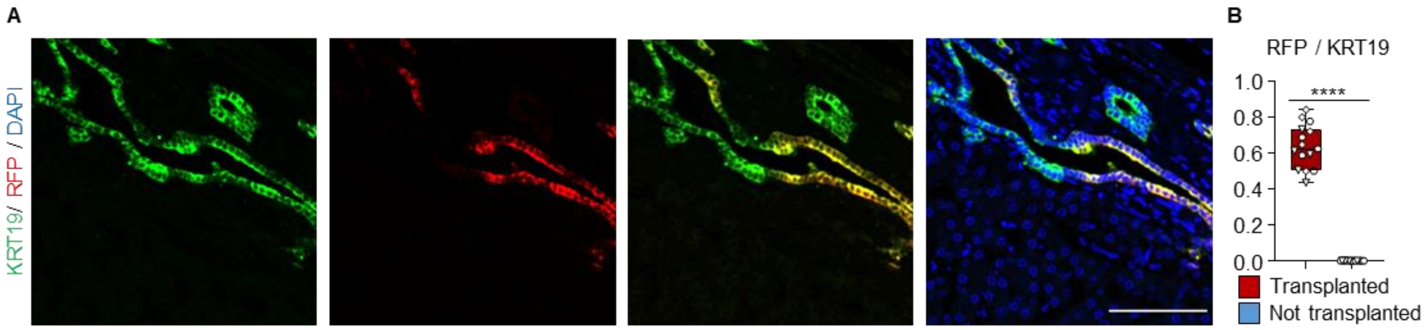

Fig. S16

Engraftment of gallbladder organoids in human livers receiving Normothermic Perfusion (NMP). (A) Immunofluorescence analysis demonstrating engraftment of human Red Fluorescent Protein (RFP) expressing cells following transplantation in NMP human livers. Scale bars, 100µm. The images are complementary to **Fig. 4, S15**. **(B)** Quantification of gallbladder-derived RFP-expressing cells in injected vs. not injected human bile ducts; **** $P<0.0001$, Mann-Whitney test. The data corresponds to 3 different livers and 5 random sections per liver. Each section is represented by a data point, while each organ is represented by a different symbol.

Table S1.

Table of the number of animals at risk corresponding to the Kaplan-Meier curve in **Fig. 3B**.

Days	**Number of animals at risk**	
	Organoids	*Carrier*
0	5	5
5	5	5
8	5	4
16	5	3
17	5	2
18	5	1
59	5	0
92	4	0

Table S2.

Table of antibodies used.

Antibody	**Provider**	**Catalogue number**	**Dilution**	**Species**
Anti-FGF19	Santa Cruz	sc-390621	1:100	Mouse
Anti-FGF19	Abcam	ab225942	1:100	Rabbit
Anti-TFF2	R&D systems	MAB4077	1:50	Mouse
Anti-DCDC2	Santa Cruz	sc-166051	1:100	Mouse
Anti-human albumin	R&D systems	MAB1455	1:50	Mouse
Anti-SOX4	Abcam	ab86809	1:50	Rabbit
Anti-SOX17	R&D systems	AF1924	1:100	Goat
Anti-RFP	Abcam	ab62341	1:100	Rabbit
Anti-RFP	Rockland	200-101-379	1:200	Goat
Anti-KRT19	DSHB	TROMA III	1:100	Rat
Anti-KRT19	Abcam	ab7754	1:100	Mouse
Anti-KRT19	Abcam	ab52625	1:100	Rabbit
Anti-KRT7	DAKO	GA61961-2	1:100	Mouse
Anti-KRT7	Abcam	ab68459	1:100	Rabbit
Anti-αSMA	DAKO	GA61161-2	1:100	Mouse
HNF1B (c-20)	SANTA CRUZ	sc-7411	1:100	Goat
GAMMA-GLUTAMYL TRANSPEPTIDASE (GGT)	Abcam	ab55138	1:100	Mouse
CYSTIC FIBROSIS TRANSMEMBRANE CONDUCTANCE REGULATOR (CFTR)	SANTA CRUZ	sc-10747	1:100	Rabbit
ALEXA FLUOR DONKEY ANTI-Rabbit 568	A10042	INVITROGEN	1:1000	Donkey
ALEXA FLUOR DONKEY ANTI-Rabbit 488	A21206	INVITROGEN	1:1000	Donkey
ALEXA FLUOR DONKEY ANTI-Rabbit 647	A31573	INVITROGEN	1:1000	Donkey
ALEXA FLUOR DONKEY ANTI-goat 568	A11057	INVITROGEN	1:1000	Donkey
ALEXA FLUOR DONKEY ANTI-goat 488	A11055	INVITROGEN	1:1000	Donkey
ALEXA FLUOR DONKEY ANTI-goat 647	A21447	INVITROGEN	1:1000	Donkey
ALEXA FLUOR DONKEY ANTI-mouse 568	A10037	INVITROGEN	1:1000	Donkey
ALEXA FLUOR DONKEY ANTI-mouse 488	A21202	INVITROGEN	1:1000	Donkey
ALEXA FLUOR DONKEY ANTI-mouse 647	A31571	INVITROGEN	1:1000	Donkey

Table S3

Table of QPCR primers used.

Gene	Primer sequence (5’ à 3’)	
HNF1B	F	TCACAGATACCAGCAGCATCAGT
	R	GGGCATCACCAGGCTTGTA
PBGD	F	GGAGCCATGTCTGGTAACGG
	R	CCACGCGAATCACTCTCATCT
SOX9	F	CTCTGGAGACTTCTGAACGAGAG
	R	CCTTGAAGATGGCGTTGGGG
CK19	F	ACGACCATCCAGGACCTGCGG
	R	TCCCACTTGGCCCCTCAGCGTA
CK7	F	GATTGCTGGCCTTCGGGGT
	R	TCATCACAGAGATATTCACGGCTC
GGT	F	GTGAGAGCAGTTGGCTGTGC
	R	GTTGAACTCTGCTGTGGGGC
CFTR	F	AGTTGCAGATGAGGTTGGGC
	R	AAAGAGCTTCACCCTGTCGG
SOX4	F	AGCGACAAGATCCCTTTCATTC
	R	CGTTGCCGGACTTCACCTT
TFF2	F	CCCATAACAGGACGAACTGC
	R	GCACTGATCCGACTCTTGCT
SOX17	F	CGCACGGAATTTGAACAGTA
	R	GGATCAGGGACCTGTCACAC
FGF19	F	ATGCAGGGGCTGCTTCAGTA
	R	AGCCATCTGGGCGGATCT

Movie S1.

T1 weighted Magnetic Resonance Imaging (MRI) of a control mouse, receiving MDA followed by injection of carrier medium without organoids in the biliary tree.

Movie S2.

T2 weighted MRI/ Magnetic Resonance CholangioPancreatography (MRCP) of a control mouse receiving MDA followed by injection of carrier medium without organoids in the biliary tree demonstrating the presence of cholangiopathy. The MRCP sequence corresponds to the reconstructed MRCP image in Fig. 3C (not transplanted panel).

Movie S3.

T1 weighted Magnetic Resonance Imaging (MRI) of a mouse receiving MDA followed by injection of organoids in the biliary tree. The images were acquired 90 days after the injection of organoids demonstrating normal liver anatomy with no formation of tumors.

Movie S4.

T2 weighted MRI/ Magnetic Resonance CholangioPancreatography (MRCP) of a mouse receiving MDA followed by injection of organoids in the biliary tree demonstrating resolution of cholangiopathy. The MRCP sequence corresponds to the reconstructed MRCP image in **Fig. 3C** (transplanted panel).

Movie S5

MRI-based 3D reconstruction of the biliary tree of a control mouse receiving MDA followed by injection of carrier medium without organoids in the biliary tree demonstrating the presence of cholangiopathy with loss of bile duct signal. The bile ducts were reconstructed from T2 weighted MR images.

Movie S6

MRI-based 3D reconstruction of the biliary tree of a mouse receiving MDA followed by injection of organoids in the biliary tree demonstrating resolution of cholangiopathy. The bile ducts were reconstructed from T2 weighted MR images.

Movie S7

Z-stack of native and regenerated RFP-expressing bile ducts in the liver of an animal receiving MDA followed by injection of RFP-expressing human gallbladder organoids in the biliary tree. KRT19 is shown in green. RFP is shown in red. The movie is complementary to **movies S8** and **S9**.

Movie S8

3D reconstruction illustrating native and regenerated bile ducts in the liver of an animal receiving MDA followed by injection of RFP-expressing human gallbladder organoids in the biliary tree. Native ducts, KRT19 positive/ RFP negative; regenerated ducts, KRT19 positive/ RFP positive. The bile ducts were reconstructed from the RFP and KRT19 immunofluorescence images used to generate **movie S7**. KRT19 is shown in green, RFP is shown in red. The movie is complementary to **movies S7** and **S9**.

Movie S9

3D rendering illustrating native and regenerated bile ducts in the liver of an animal receiving MDA followed by injection of RFP-expressing human gallbladder organoids in the biliary tree. Native ducts, KRT19 positive/ RFP negative; regenerated ducts, KRT19 positive/ RFP positive. The bile ducts were reconstructed from the RFP and KRT19 immunofluorescence images used to generate **movie S7** and **S8**. KRT19 is shown in green, RFP is shown in red. The movie is complementary to **movies S7** and **S8**.

Data S1. (separate file)

Table of differentially expressed genes between different regions of the biliary tree. IHD, Intrahepatic ducts; CBD, Common Bile Duct; GB, Gallbladder. The table corresponds to genes with a log2 fold change > 1 and an adjusted P value < 0.001.

Data S2. (separate file)

Table of differentially expressed genes in pseudotime in primary cholangiocytes with an adjusted P value<0.001.

Data S3. (separate file)

Table of differentially expressed genes upregulated in organoids or organoids treated with bile versus primary cholangiocytes. ORG, organoids; ORGT, Bile treated organoids. The table corresponds to genes with a log2 fold change > 1 and an adjusted P value < 0.001.

References and notes

1. J. Drost, H. Clevers, Translational applications of adult stem cell-derived organoids. *Development* **144**, 968–975 (2017). doi:10.1242/dev.140566 Medline

2. R. H. Squires, V. Ng, R. Romero, U. Ekong, W. Hardikar, S. Emre, G. V. Mazariegos, Evaluation of the pediatric patient for liver transplantation: 2014 practice guideline by the American Association for the Study of Liver Diseases, American Society of Transplantation and the North American Society for Pediatric Gastroenterology, Hepatology and Nutrition. *Hepatology* **60**, 362–398 (2014). doi:10.1002/hep.27191 Medline

3. F. Sampaziotis, A. W. Justin, O. C. Tysoe, S. Sawiak, E. M. Godfrey, S. S. Upponi, R. L. Gieseck 3rd, M. C. de Brito, N. L. Berntsen, M. J. Gómez-Vázquez, D. Ortmann, L. Yiangou, A. Ross, J. Bargehr, A. Bertero, M. C. F. Zonneveld, M. T. Pedersen, M. Pawlowski, L. Valestrand, P. Madrigal, N. Georgakopoulos, N. Pirmadjid, G. M. Skeldon, J. Casey, W. Shu, P. M. Materek, K. E. Snijders, S. E. Brown, C. A. Rimland, I. Simonic, S. E. Davies, K. B. Jensen, M. Zilbauer, W. T. H. Gelson, G. J. Alexander, S. Sinha, N. R. F. Hannan, T. A. Wynn, T. H. Karlsen, E. Melum, A. E. Markaki, K. Saeb-Parsy, L. Vallier, Reconstruction of the mouse extrahepatic biliary tree using primary human extrahepatic cholangiocyte organoids. *Nat. Med.* **23**, 954–963 (2017). doi:10.1038/nm.4360 Medline

4. K. Parikh, A. Antanaviciute, D. Fawkner-Corbett, M. Jagielowicz, A. Aulicino, C. Lagerholm, S. Davis, J. Kinchen, H. H. Chen, N. K. Alham, N. Ashley, E. Johnson, P. Hublitz, L. Bao, J. Lukomska, R. S. Andev, E. Björklund, B. M. Kessler, R. Fischer, R. Goldin, H. Koohy, A. Simmons, Colonic epithelial cell diversity in health and inflammatory bowel disease. *Nature* **567**, 49–55 (2019). doi:10.1038/s41586-019-0992-y Medline

5. C. A. Rimland, S. G. Tilson, C. M. Morell, R. A. Tomaz, W.-Y. Lu, S. E. Adams, N. Georgakopoulos, F. Otaizo-Carrasquero, T. G. Myers, J. R. Ferdinand, R. L. Gieseck 3rd, F. Sampaziotis, O. C. Tysoe, B. Wesley, D. Muraro, G. C. Oniscu, N. R. Hannan, S. J. Forbes, K. Saeb-Parsy, T. A. Wynn, L. Vallier, Regional differences in human biliary tissues and corresponding *in vitro* derived organoids. *Hepatology* 10.1002/hep.31252 (2020). doi:10.1002/hep.31252 Medline

6. J. H. Tabibian, A. I. Masyuk, T. V. Masyuk, S. P. O'Hara, N. F. LaRusso, Physiology of cholangiocytes. *Compr. Physiol.* **3**, 541–565 (2013). doi:10.1002/cphy.c120019 Medline

7. A. I. Masyuk, N. F. LaRusso, Aquaporins in the hepatobiliary system. *Hepatology* **43**, S75–S81 (2006). doi:10.1002/hep.20996 Medline

8. K.-S. Yoo, H. S. Choi, D. W. Jun, H. L. Lee, O. Y. Lee, B. C. Yoon, K. G. Lee, S. S. Paik, Y. S. Kim, J. Lee, MUC Expression in Gallbladder Epithelial Tissues in Cholesterol-Associated Gallbladder Disease. *Gut Liver* **10**, 851–858 (2016). doi:10.5009/gnl15600 Medline

9. S. J. L. B. Zweers, K. A. C. Booij, M. Komuta, T. Roskams, D. J. Gouma, P. L. M. Jansen, F. G. Schaap, The human gallbladder secretes fibroblast growth factor 19 into bile: Towards defining the role of fibroblast growth factor 19 in the enterobiliary tract. *Hepatology* **55**, 575–583 (2012). doi:10.1002/hep.24702 Medline

10. Y. Zong, B. Z. Stanger, Molecular mechanisms of bile duct development. *Int. J. Biochem. Cell Biol.* **43**, 257–264 (2011). doi:10.1016/j.biocel.2010.06.020 Medline

11. K. Si-Tayeb, F. P. Lemaigre, S. A. Duncan, Organogenesis and development of the liver. *Dev. Cell* **18**, 175–189 (2010). doi:10.1016/j.devcel.2010.01.011 Medline

12. N. Aizarani, A. Saviano, L. Sagar, L. Mailly, S. Durand, J. S. Herman, P. Pessaux, T. F. Baumert, D. Grün, A human liver cell atlas reveals heterogeneity and epithelial progenitors. *Nature* **572**, 199–204 (2019). doi:10.1038/s41586-019-1373-2 Medline

13. B. J. Pepe-Mooney, M. T. Dill, A. Alemany, J. Ordovas-Montanes, Y. Matsushita, A. Rao, A. Sen, M. Miyazaki, S. Anakk, P. A. Dawson, N. Ono, A. K. Shalek, A. van Oudenaarden, F. D. Camargo, Single-Cell Analysis of the Liver Epithelium Reveals Dynamic Heterogeneity and an Essential Role for YAP in Homeostasis and Regeneration. *Cell Stem Cell* **25**, 23–38.e8 (2019). doi:10.1016/j.stem.2019.04.004 Medline

14. L. Planas-Paz, T. Sun, M. Pikiolek, N. R. Cochran, S. Bergling, V. Orsini, Z. Yang, F. Sigoillot, J. Jetzer, M. Syed, M. Neri, S. Schuierer, L. Morelli, P. S. Hoppe, W. Schwarzer, C. M. Cobos, J. L. Alford, L. Zhang, R. Cuttat, A. Waldt, N. Carballido-Perrig, F. Nigsch, B. Kinzel, T. B. Nicholson, Y. Yang, X. Mao, L. M. Terracciano, C. Russ, J. S. Reece-Hoyes, C. Gubser Keller, A. W. Sailer, T. Bouwmeester, L. E. Greenbaum, J. J. Lugus, F. Cong, G. McAllister, G. R. Hoffman, G. Roma, J. S. Tchorz, YAP, but Not RSPO-LGR4/5, Signaling in Biliary Epithelial Cells Promotes a Ductular Reaction in Response to Liver Injury. *Cell Stem Cell* **25**, 39–53.e10 (2019). doi:10.1016/j.stem.2019.04.005 Medline

15. A. Lanzini, in *Encyclopedia of Food Sciences and Nutrition*, B. Caballero, Ed. (Academic Press, ed. 2, 2003), pp. 471–478.

16. O. C. Tysoe, A. W. Justin, T. Brevini, S. E. Chen, K. T. Mahbubani, A. K. Frank, H. Zedira, E. Melum, K. Saeb-Parsy, A. E. Markaki, L. Vallier, F. Sampaziotis, Isolation and propagation of primary human cholangiocyte organoids for the generation of bioengineered biliary tissue. *Nat. Protoc.* **14**, 1884–1925 (2019). doi:10.1038/s41596-019-0168-0 Medline

17. S.-B. Kwon, J.-S. Park, J.-Y. Yi, J.-W. Hwang, M. Kim, M.-O. Lee, B.-H. Lee, H.-L. Kim, J. H. Kim, H. Chung, G. Kong, K.-S. Kang, B.-I. Yoon, Time- and dose-based gene expression profiles produced by a bile-duct-damaging chemical, 4,4′-methylene dianiline, in mouse liver in an acute phase. *Toxicol. Pathol.* **36**, 660–673 (2008). doi:10.1177/0192623308320272 Medline

18. N. L. Berntsen, B. Fosby, L. Valestrand, C. Tan, H. M. Reims, E. Schrumpf, T. H. Karlsen, P. D. Line, E. Melum, Establishment of a surgical bile duct injection technique giving direct access to the bile ducts for studies of the murine biliary tree. *Am. J. Physiol. Gastrointest. Liver Physiol.* **314**, G349–G359 (2018). doi:10.1152/ajpgi.00124.2017 Medline

19. C. Arber, M. K. Brenner, P. Reddy, Mouse models in bone marrow transplantation and adoptive cellular therapy. *Semin. Hematol.* **50**, 131–144 (2013). doi:10.1053/j.seminhematol.2013.03.026 Medline

20. D. Nasralla, C. C. Coussios, H. Mergental, M. Z. Akhtar, A. J. Butler, C. D. L. Ceresa, V. Chiocchia, S. J. Dutton, J. C. García-Valdecasas, N. Heaton, C. Imber, W. Jassem, I. Jochmans, J. Karani, S. R. Knight, P. Kocabayoglu, M. Malagò, D. Mirza, P. J. Morris, A. Pallan, A. Paul, M. Pavel, M. T. P. R. Perera, J. Pirenne, R. Ravikumar, L.

Russell, S. Upponi, C. J. E. Watson, A. Weissenbacher, R. J. Ploeg, P. J. Friend, Consortium for Organ Preservation in Europe, A randomized trial of normothermic preservation in liver transplantation. *Nature* **557**, 50–56 (2018). doi:10.1038/s41586-018-0047-9 Medline

21. A. I. Skaro, C. L. Jay, T. B. Baker, E. Wang, S. Pasricha, V. Lyuksemburg, J. A. Martin, J. M. Feinglass, L. B. Preczewski, M. M. Abecassis, The impact of ischemic cholangiopathy in liver transplantation using donors after cardiac death: The untold story. *Surgery* **146**, 543–553 (2009). doi:10.1016/j.surg.2009.06.052 Medline

22. C. K. Enestvedt, S. Malik, P. P. Reese, A. Maskin, P. S. Yoo, S. A. Fayek, P. Abt, K. M. Olthoff, A. Shaked, Biliary complications adversely affect patient and graft survival after liver retransplantation. *Liver Transpl.* **19**, 965–972 (2013). doi:10.1002/lt.23696 Medline

23. C. J. E. Watson, V. Kosmoliaptsis, C. Pley, L. Randle, C. Fear, K. Crick, A. E. Gimson, M. Allison, S. Upponi, R. Brais, I. Jochmans, A. J. Butler, Observations on the ex situ perfusion of livers for transplantation. *Am. J. Transplant.* **18**, 2005–2020 (2018). doi:10.1111/ajt.14687 Medline

24. R. G. Farmer, W. A. Hawk, R. B. Turnbull Jr., Clinical patterns in Crohn's disease: A statistical study of 615 cases. *Gastroenterology* **68**, 627–635 (1975). Medline

25. S. A. MacParland, J. C. Liu, X. Z. Ma, B. T. Innes, A. M. Bartczak, B. K. Gage, J. Manuel, N. Khuu, J. Echeverri, I. Linares, R. Gupta, M. L. Cheng, L. Y. Liu, D. Camat, S. W. Chung, R. K. Seliga, Z. Shao, E. Lee, S. Ogawa, M. Ogawa, M. D. Wilson, J. E. Fish, M. Selzner, A. Ghanekar, D. Grant, P. Greig, G. Sapisochin, N. Selzner, N. Winegarden, O. Adeyi, G. Keller, G. D. Bader, I. D. McGilvray, Single cell RNA sequencing of human liver reveals distinct intrahepatic macrophage populations. *Nat. Commun.* **9**, 4383 (2018). doi:10.1038/s41467-018-06318-7 Medline

26. D. J. McCarthy, K. R. Campbell, A. T. L. Lun, Q. F. Wills, Scater: Pre-processing, quality control, normalization and visualization of single-cell RNA-seq data in R. *Bioinformatics* **33**, 1179–1186 (2017). doi:10.1093/bioinformatics/btw777 Medline

27. A. Butler, P. Hoffman, P. Smibert, E. Papalexi, R. Satija, Integrating single-cell transcriptomic data across different conditions, technologies, and species. *Nat. Biotechnol.* **36**, 411–420 (2018). doi:10.1038/nbt.4096 Medline

28. L. Haghverdi, A. T. L. Lun, M. D. Morgan, J. C. Marioni, Batch effects in single-cell RNA-sequencing data are corrected by matching mutual nearest neighbors. *Nat. Biotechnol.* **36**, 421–427 (2018). doi:10.1038/nbt.4091 Medline

29. F. A. Wolf, P. Angerer, F. J. Theis, SCANPY: Large-scale single-cell gene expression data analysis. *Genome Biol.* **19**, 15 (2018). doi:10.1186/s13059-017-1382-0 Medline

30. L. Haghverdi, M. Büttner, F. A. Wolf, F. Buettner, F. J. Theis, Diffusion pseudotime robustly reconstructs lineage branching. *Nat. Methods* **13**, 845–848 (2016). doi:10.1038/nmeth.3971 Medline

31. X. Qiu, Q. Mao, Y. Tang, L. Wang, R. Chawla, H. A. Pliner, C. Trapnell, Reversed graph embedding resolves complex single-cell trajectories. *Nat. Methods* **14**, 979–982 (2017). doi:10.1038/nmeth.4402 Medline

32. V. Y. Kiselev, K. Kirschner, M. T. Schaub, T. Andrews, A. Yiu, T. Chandra, K. N. Natarajan, W. Reik, M. Barahona, A. R. Green, M. Hemberg, SC3: Consensus

clustering of single-cell RNA-seq data. *Nat. Methods* **14**, 483–486 (2017). doi:10.1038/nmeth.4236 Medline

33. L. Zappia, A. Oshlack, Clustering trees: A visualization for evaluating clusterings at multiple resolutions. *Gigascience* **7**, giy083 (2018). doi:10.1093/gigascience/giy083 Medline

34. A. Subramanian, P. Tamayo, V. K. Mootha, S. Mukherjee, B. L. Ebert, M. A. Gillette, A. Paulovich, S. L. Pomeroy, T. R. Golub, E. S. Lander, J. P. Mesirov, Gene set enrichment analysis: A knowledge-based approach for interpreting genome-wide expression profiles. *Proc. Natl. Acad. Sci. U.S.A.* **102**, 15545–15550 (2005). doi:10.1073/pnas.0506580102 Medline

35. M. V. Kuleshov, M. R. Jones, A. D. Rouillard, N. F. Fernandez, Q. Duan, Z. Wang, S. Koplev, S. L. Jenkins, K. M. Jagodnik, A. Lachmann, M. G. McDermott, C. D. Monteiro, G. W. Gundersen, A. Ma'ayan, Enrichr: A comprehensive gene set enrichment analysis web server 2016 update. *Nucleic Acids Res.* **44**, W90–W97 (2016). doi:10.1093/nar/gkw377 Medline

36. F. Sampaziotis, M. C. de Brito, P. Madrigal, A. Bertero, K. Saeb-Parsy, F. A. C. Soares, E. Schrumpf, E. Melum, T. H. Karlsen, J. A. Bradley, W. T. H. Gelson, S. Davies, A. Baker, A. Kaser, G. J. Alexander, N. R. F. Hannan, L. Vallier, Cholangiocytes derived from human induced pluripotent stem cells for disease modeling and drug validation. *Nat. Biotechnol.* **33**, 845–852 (2015). doi:10.1038/nbt.3275 Medline

37. F. Sampaziotis, M. C. de Brito, I. Geti, A. Bertero, N. R. Hannan, L. Vallier, Directed differentiation of human induced pluripotent stem cells into functional cholangiocyte-like cells. *Nat. Protoc.* **12**, 814–827 (2017). doi:10.1038/nprot.2017.011 Medline

38. R. Ravikumar, W. Jassem, H. Mergental, N. Heaton, D. Mirza, M. T. P. R. Perera, A. Quaglia, D. Holroyd, T. Vogel, C. C. Coussios, P. J. Friend, Liver Transplantation After Ex Vivo Normothermic Machine Preservation: A Phase 1 (First-in-Man) Clinical Trial. *Am. J. Transplant.* **16**, 1779–1787 (2016). doi:10.1111/ajt.13708 Medline